Acta Materialia 288 (2025) 120816

Contents lists available at ScienceDirect

Acta Materialia

journal homepage: www.elsevier.com/locate/actamat

Full length article

Defects caused by powder spattering and entrainment in laser powder bed fusion process: High-fidelity modeling of gas, melt pool and powder dynamics

Yanming Zhang [a], Shiwei Wu [a], Zixu Guo [a], Guochen Peng [a], Lu Wang [b], Wentao Yan [a,*]

[a] Department of Mechanical Engineering, National University of Singapore, 117575, Singapore
[b] Department of Mechanical Engineering, City University of Hong Kong, 999077, Hong Kong, China

ARTICLE INFO

Keywords:
Additive manufacturing
Laser powder bed fusion
Defect
Powder spattering and entrainment
Multi-physics modeling
Gas-melt pool-powder dynamics

ABSTRACT

Inconsistent product quality is one of the major bottlenecks hindering the widespread adoption of laser powder bed fusion (LPBF) additive manufacturing technology in various industries. A vital source of the inconsistency is the defect caused by the powder spattering and entrainment in the melting process. However, the mechanisms of defect formation remain elusive due to the highly-dynamic nature of multiphase flow. Here we develop a multi-physics simulation model, together with experiment validations, to simultaneously elucidate the gas, melt pool and particle dynamics in the melting process. The high-fidelity simulations successfully uncover the mechanisms of defect formation. In particular, the large agglomeration induced by the hot spatter coalescence can probably induce lack-of-fusion and porosity defects. The powder entrainment can probably cause particle inclusion defects in multi-material LPBF. Moreover, the momentum of entrained particles can alter the flow field at the melt pool tail. Under the guidance of simulation, we propose the criterion of defect generation in the melting process, which is beneficial to the real-time detection and mitigation of defects. The deep insights into the defects caused by powder spattering and entrainment provide valuable guidance for improving the consistency of LPBF parts.

1. Introduction

The recent decade has witnessed the remarkable development of metal additive manufacturing (AM) toward a manufacturing technology for end-use components [1–3]. As a prevalent AM technique, laser powder bed fusion (LPBF) offers a promising pathway to produce bespoke parts with complex structures and multiple functionalities [4–6]. However, a longstanding issue for LPBF is the inconsistent product quality. Despite enormous efforts of optimizing primary processing parameters (e.g., laser power, scan speed and hatching pattern), LPBF parts still exhibit inconsistent qualities under the optimized primary processing parameters, which hinders the widespread adoption of LPBF in various industries such as the automotive, aviation and nuclear energy industries [7,8].

A vital source of inconsistent product quality is the defect caused by powder spattering and entrainment in the melting process [9,10]. As the laser irradiates on the surface of metallic material, the localized laser heating triggers intensive metal evaporation and produces a high-speed vapor jet. The powder particles near the vapor jet are rapidly blown up to form spatters. Meanwhile, the ambient gas is pushed toward the vapor jet region and causes powder entrainment [11,12]. Previous studies have found the re-deposition of spatters on the powder bed can significantly increase the lack-of-fusion and porosity defects in the LPBF parts [13–16]. These defects are difficult to eliminate by optimizing the primary processing parameters. Moreover, the specific positions of these defects are hard to predict due to the highly dynamic nature of powder flow. This is quite different with the defects that are determined by the primary processing parameters, such as the lack-of-fusion defects caused by the large hatch spacing [9]. The complexity of defects caused by powder spattering and entrainment poses significant challenges to investigating the defect formation mechanisms with experimental techniques. The state-of-the-art in-situ monitoring techniques, such as the high-speed optical and X-ray imaging techniques, have achieved great success in observing the vapor, particle and melt pool dynamics in the melting process [11,17–21]. However, the formation process of defects caused by powder spattering and entrainment is still difficult to capture due to limitations of imaging systems.

* Corresponding author.
E-mail address: mpeyanw@nus.edu.sg (W. Yan).

https://doi.org/10.1016/j.actamat.2025.120816
Received 16 September 2024; Received in revised form 7 January 2025; Accepted 7 February 2025
Available online 17 February 2025

On the other hand, numerical simulation is becoming a powerful tool to reveal the multiphase dynamics in the melting process. Previous studies mainly applied the Discrete Element Method (DEM) to simulate the powder spreading process [22] and the generated powder bed was transferred to the Computational Fluid Dynamic (CFD) model to simulate the melt pool dynamics. A wide range of physical phenomena have been reproduced by CFD models, such as balling effect [23], keyhole pore generation [24,25], vapor ejection [26] and liquid spattering [27]. However, due to the decoupling of CFD and DEM models, these simulation models cannot reproduce the motion of powder particles in the melting process. Recently, a few researchers have developed CFD–DEM coupling models to simultaneously reproduce the gas, melt pool and particle dynamics, which provide important insights into the multiphase flow at the beginning of melt track [28–30]. Nevertheless, the lack of some fluid–particle interactions (e.g., wetting effect) causes abnormal particle motion in these CFD–DEM models, making them difficult to elucidate the defects caused by powder spattering and entrainment.

In the present work, we develop a CFD–DEM-CALPHAD coupling model to simultaneously reveal the gas, melt pool and particle dynamics in single- and multi-material LPBF process. Our model is validated against the in-situ and post-processing experiments with different materials and processing parameters. Through high-fidelity simulations, we clearly elucidate formation mechanisms of defects induced by powder spattering and entrainment. Under the guidance of simulations, we propose the criterion of defect generation in the melting process, which is beneficial to the real-time detection and mitigation of defects caused by powder spattering and entrainment. Our work provides valuable guidance for improving the consistency of LPBF parts.

2. Methodology

2.1. CFD model: fluid dynamics

In this study, the mixture fluid model is employed to model the transport of different elements in liquid and gas phases [31]. The basic assumptions of the CFD model are listed as follows:

(I) The liquid and gas are assumed to be incompressible Newtonian fluid.
(II) The mass diffusion of chemical elements in the melt pool is minor and thus ignored.
(III) The influence of vapor plume on laser propagation is not considered in the present work. These assumptions are justified and discussed in the supplementary materials.

The mass equation of element k is:

$$\frac{\partial C_k}{\partial t} + \nabla \cdot (C_k \vec{U}) = \dot{m}_k \tag{1}$$

where $\vec{U} = (U_1, U_2, U_3)$ is the fluid velocity. C_k is the mass concentration of element k (unit: kg/m^3). $\dot{m}_k$ is the mass source of element k (e.g., vapor ejection due to evaporation). The momentum equation is:

$$\frac{\partial(\rho\vec{U})}{\partial t} + \nabla \cdot (\rho\vec{U}\vec{U}) = \nabla \cdot \boldsymbol{S} + \rho\vec{g} + \sum_k \dot{m}_k \vec{u}_k \tag{2}$$

where $\rho = \sum_k C_k$ is the density of fluid. $\vec{g}$ is gravitational acceleration and $\vec{u}_k$ is the velocity of mass source of element k. $\boldsymbol{S}$ is the stress tensor of fluid, which is given as:

$$S_{ij} = -\left(p + \frac{2}{3}\mu\nabla \cdot \vec{U}\right)\delta_{ij} + \mu\left(\frac{\partial U_i}{\partial x_j} + \frac{\partial U_j}{\partial x_i}\right) \quad i, j \in 1, 2, 3 \tag{3}$$

where p is the pressure, δ_{ij} is the Kronecker delta function and μ is the dynamic viscosity of fluid. In the present work, μ is calculated based on the mole fraction average of those of the elements. To model the effect of solidification on fluidity, a constant finite viscosity much larger than that of the liquid phase is assigned to the solid phase. The thermal energy equation is:

$$\frac{\partial(\rho I_f)}{\partial t} + \nabla \cdot (\rho I_f \vec{U}) = -p(\nabla \cdot \vec{U}) + \nabla \cdot (K\nabla T) + \sum_k \dot{m}_k I_k + Q_f \tag{4}$$

where I_f is the internal energy of fluid and I_k is the internal energy of the element k from mass source. T and K are the temperature and thermal conductivity of fluid, respectively. Q_f is the heat source energy absorbed by fluid. In the present study, the ray tracing model is implemented to trace the laser propagation [32]. The laser beam is subdivided into a series of rays, and the absorptivity of each ray at each reflection is calculated by the Fresnel equation. The equivalent refractive index of material containing multiple elements is calculated by Maxwell–Garnett mixing formula [33]. The volume of fluid (VoF) method is applied to track the free surface of melt pool [34]:

$$\frac{\partial F}{\partial t} + \nabla \cdot (F\vec{U}) = \sum_k \frac{\dot{m}_k}{\rho_k} \tag{5}$$

where F is the volume fraction of liquid, and ρ_k is the bulk density of element k.

The accurate modeling of vapor ejection during evaporation is essential to reproduce the multiphase dynamics in the melting process. In the present work, the evaporation model developed in our previous study is incorporated to quantitatively reproduce the mass, momentum and energy fluxes of vapor jet [35]. The flow structure near the liquid–gas interface are shown in Fig. 1. The mass, momentum and energy sources carried by evaporated element k are given as:

$$\begin{cases} \dot{m}_k = \dfrac{A_l}{V_g}\rho_{3,k}u_{3,k} \\ \dot{m}_k\vec{u}_k = \dfrac{A_l}{V_g}(\rho_{3,k}u_{3,k}^2 + \rho_{3,k}R_{3,k}T_{3,k})\vec{n} \\ \dot{m}_k I_k = \dfrac{A_l}{2V_g}\rho_{3,k}u_{3,k}(u_{3,k}^2 + 5R_{3,k}T_{3,k}) \end{cases} \tag{6}$$

where A_l is the area of local melt pool surface and V_g is the volume of gas phase in the mesh cell. The term A_l/V_g in Eq. (6) is to convert the surface flux to the volumetric source. $\vec{n}$ is the unit normal vector outward the liquid surface. $\rho_{3,k}$, $u_{3,k}$, $R_{3,k}$ and $T_{3,k}$ are the density, velocity, gas constant and temperature of vapor at region III shown in Fig. 1 respectively, which are calculated based on the temperature of local melt pool surface and pressure/temperature of ambient gas.

For the force boundary conditions on the free surface of melt pool, the recoil pressure ($\vec{f}_{rec}$), Laplace pressure ($\vec{f}_l$), Marangoni force ($\vec{f}_t$) and wetting force ($\vec{f}_w$) are considered, which are given as:

$$\begin{cases} \vec{f}_{rec} = -\sum_k(\rho_{3,k}u_{3,k}^2 + \rho_{3,k}R_{3,k}T_{3,k})\vec{n} \\ \vec{f}_l = \gamma\kappa\vec{n} \\ \vec{f}_t = -\dfrac{\mathrm{d}\gamma}{\mathrm{d}T}[\nabla T - (\nabla T \cdot \vec{n})\vec{n}] \\ \vec{f}_w = \gamma_{lg}(\cos\theta - \cos\theta_e)\vec{t} \end{cases} \tag{7}$$

$\vec{f}_{rec}$ is essentially the anti-momentum flux caused by the vapor ejection [35]. $\vec{f}_l$ is induced by the local interface curvature (κ). In the present work, the parabolic fitting plus the height function method is applied to calculate κ [36]. $\gamma = \gamma_0 - \frac{\mathrm{d}\gamma}{\mathrm{d}T}(T - T_0)$ is the interface energy, where γ_0 is interface energy at temperature T_0 and $\frac{\mathrm{d}\gamma}{\mathrm{d}T}$ is the temperature sensitivity [37]. The wetting force model is used to reproduce the wetting effect at the three-phase interface [38]. $\vec{t}$ is the unit vector normal to the local contact line within the tangential plane of powder particle. θ and θ_e are the current and equilibrium contact angle on the gas-liquid–solid interface, given as:

$$\begin{cases} \cos\theta_e = \dfrac{\gamma_{sg} - \gamma_{sl}}{\gamma_{lg}} \\ \cos\theta = -\vec{n} \cdot \vec{n}_p \end{cases} \tag{8}$$

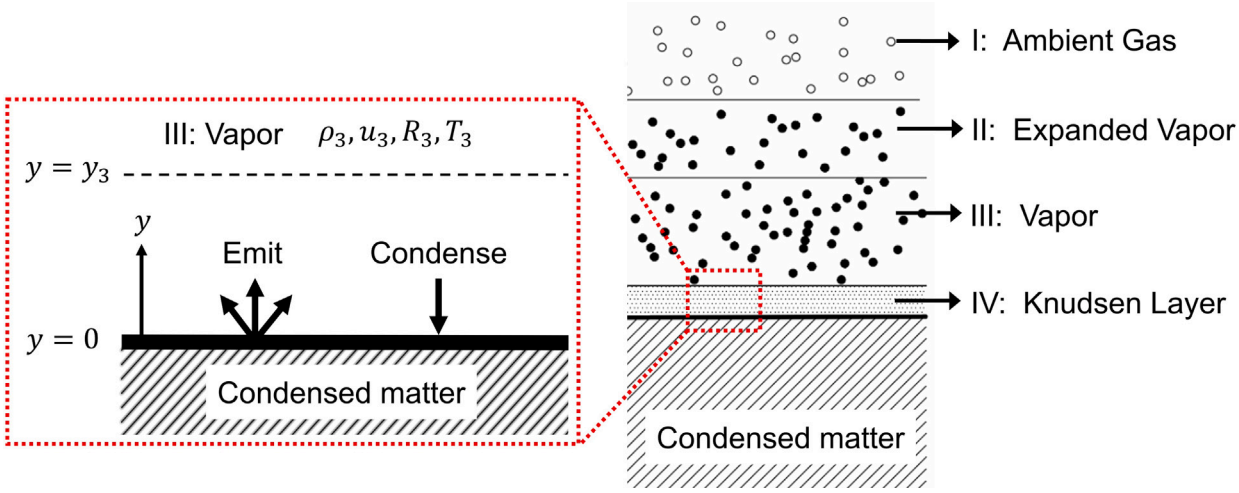

Fig. 1. Schematic diagram of gas flow structure in the evaporation model [35]. The red box on the left shows the detailed structure of the Knudsen layer above the melt pool surface (region IV). (For interpretation of the references to color in this figure legend, the reader is referred to the web version of this article.)

where $\vec{n}_p$ is the unit normal vector outward the surface of solid particle. γ_{sg}, γ_{sl} and γ_{lg} are the solid–gas, solid–liquid and liquid–gas interface energy, respectively. In the present work, the influence of surface texture of powder particle on the wettability is not incorporated. The thermal boundary condition is given as:

$$-K\nabla T\cdot\vec{n} = h_{lg}(T-T_a) + \epsilon\delta_s(T^4-T_a^4) + \sum_k \dot{m}_k L_{v,k} \tag{9}$$

where h_{lg} is the convective heat transfer coefficient between liquid and gas phases, δ_s is the Stefan–Boltzmann constant, ϵ is the emissivity factor and T_a is the ambient temperature. $L_{v,k}$ is the latent heat of evaporation of the element k. In the present work, the oxidation of melt is not incorporated in the simulation model.

2.2. DEM model: powder dynamics

The DEM model is employed to reproduce the dynamics of powder particle in the melting process. To save the computational cost, the rotation of particle is not incorporated in the model, as it does not make much difference in the particle trajectory. The governing equation of particle translation is:

$$m_p\vec{a}_p = \vec{F}_g + \vec{F}_f + \vec{F}_w + \sum\vec{F}_c \tag{10}$$

where m_p and $\vec{a}_p$ are the mass and acceleration of the particle. $\vec{F}_g$, $\vec{F}_w$, $\vec{F}_f$ and $\sum\vec{F}_c$ are the gravity, wetting force, fluid drag force and contact forces, respectively. The wetting force on the particle is given as:

$$\vec{F}_w = -\oint_L \vec{f}_w dL = -\oint_L \gamma_{lg}(\cos\theta-\cos\theta_e)\vec{t}dL \tag{11}$$

where L is the rim of contact line. $\vec{F}_f$ contains the undisturbed fluid force ($\vec{F}_u$), steady-state drag force ($\vec{F}_d$) and apparent mass force ($\vec{F}_a$), given as [39,40]:

$$\begin{cases} \vec{F}_u = \dfrac{1}{N}\displaystyle\sum_{i=1}^{N}\frac{m_p}{\rho_p}\nabla\cdot\boldsymbol{S} \\ \vec{F}_d = \dfrac{1}{N}\displaystyle\sum_{i=1}^{N}\frac{C_d\rho\pi r_p^2}{2}|\vec{U}-\vec{u}_p|(\vec{U}-\vec{u}_p) \\ \vec{F}_a = \dfrac{1}{N}\displaystyle\sum_{i=1}^{N}\frac{m_p}{2}\left(\frac{\mathrm{d}\vec{U}}{\mathrm{d}t}-\frac{\mathrm{d}\vec{u}_p}{\mathrm{d}t}\right) \end{cases} \tag{12}$$

where ρ_p, r_p and $\vec{u}_p$ are the density, radius and translational velocity of the particle, respectively. N is the number of mesh cells occupied by the particle. C_d is the drag force coefficient, which is given as:

$$C_d = \frac{24}{Re_p} + \frac{6}{1+\sqrt{Re_p}} + 0.4, \quad Re_p = \frac{2\rho r_p|\vec{U}-\vec{u}_p|}{\mu} \tag{13}$$

The value of C_d in Eq. (13) matches well with experiment results when the Reynolds number of fluid is smaller than 3×10^5 [39]. The anti-force $-\vec{F}_f$ is added in corresponding CFD mesh cells to represent the influence of powder particle on fluid flow. For the particles in contact (i.e., the distance between the centers of two particles are smaller than the summation of their radius), the linear spring-damping contact model is applied to calculate $\sum\vec{F}_c$ on the particle. The details about the contact forces can be found in our previous study [41].

The thermal energy equation for each powder particle is:

$$\frac{\mathrm{d}I_p}{\mathrm{d}t} = Q_{pf} + Q_l \tag{14}$$

where I_p is the internal energy of particle. Q_{pf} is the convective heat transfer between fluid and solid particle:

$$Q_{pf} = 4\pi r_p^2 h_{pf}(T-T_p) \tag{15}$$

where T_p is the temperature of particle. h_{pf} is convective heat transfer coefficient between fluid and particle, which is evaluated based on the Nusselt number correlations for solid sphere at the external fluid flow (different for gas and liquid flow) [42]. $-Q_{pf}$ is added in corresponding CFD mesh cells to represent the heat transfer from particle to fluid. Q_l is the laser energy absorbed by particle. To accurately model the interactions between particle and fluid/laser, the volume fraction of each particle in CFD mesh is calculated to reconstruct the surface of particle [43]. If the temperature of particle is above the liquidus temperature, the particle is replaced by a liquid droplet in the computational domain with the same mass, momentum and internal energy.

2.3. CALPHAD model: metallurgical reaction

The calculation of phase diagrams (CALPHAD) model is established to incorporate the metallurgical reactions among different feedstocks during the multi-material metal AM process. The basic assumptions are listed below and justified in the supplementary materials:

(I) The direction of local metallurgical reaction is toward the local equilibrium state.
(II) The characteristic time of local metallurgical reaction is close to or smaller than that of fluid convection.
(III) The material properties in each CFD mesh represent the average material properties of all phases within the mesh.

Under the above assumptions, the liquidus temperature of metallurgical products are identical with that in equilibrium state. The heat release caused by enthalpy of mixing (ΔH) is incorporated in the

simulation by the following method. In the present work, we choose the standard state (T_{sta} = 273.15 K, P_{sta} = 10^5 Pa) as reference state. The relationship between temperature T and internal energy $I_f(\vec{X},T)$ are:

$$\begin{cases} I_f(\vec{X},T) = \rho H(\vec{X},T)/M_f(\vec{X}) \\ H(\vec{X},T) = H(\vec{X},T_{sta}) + \int_{T_{sta}}^{T} C_p(\vec{X},T)dT + f_l(\vec{X},T)L_m(\vec{X}) \end{cases} \tag{16}$$

where $M_f(\vec{X})$ and $H(\vec{X},T)$ are the molar mass and specific enthalpy of material with chemical composition of $\vec{X}$, respectively. $\vec{X} = (X_1, X_2, \dots, X_n)$ is the mole fraction vector, where X_k is the mole fraction of element k. Since we choose the standard state as reference state, $H(\vec{X},T_{sta})$ equals to the standard enthalpy of formation. $C_p(\vec{X},T)$ is the specific heat capacity and $L_m(\vec{X})$ is the latent heat of fusion. $f_l(\vec{X},T)$ is the liquid phase fraction, which is zero when T is below the solidus temperature $T_s(\vec{X})$ and unit when T is above the liquidus temperature $T_l(\vec{X})$.

At the beginning of each computational time step, the temperature of material after the reaction is calculated based on the internal energy of material and the enthalpy of reactants/products. From Eq. (16), the temperature of material increases when the overall enthalpy of products is smaller than that of reactants. In this way, the temperature increase due to ΔH is incorporated in the simulation without additional computational cost. The method ensures that the internal energy of fluid is conservative before and after the reaction. Note that the reactions occurring in solidified region is not considered in present work, since the reaction rate in solid state is much lower than that in the melt pool.

In this study, $H(\vec{X},T)$, $T_s(\vec{X})$, $T_l(\vec{X})$ and other thermophysical properties of materials with various chemical compositions are obtained through the CALPHAD method with the thermodynamic database of the corresponding alloy system. Generally, the thermodynamic database comprises the Gibbs energy G of all phases in the alloy system and other thermodynamic quantities can be evaluated from G. For example, the relationship between $G(\vec{X},T)$ and $C_p(\vec{X},T)$ is:

$$C_p(\vec{X},T) = -T\left(\frac{\partial^2 G(\vec{X},T)}{\partial T^2}\right)_P \tag{17}$$

Here we take Ni-Ti system for example to illustrate the procedure of calculating the thermodynamic quantities. The Gibbs energy data is obtained from NIMS thermodynamic database, where γ-Ni, Ni3Ti, NiTi, NiTi2, α-Ti, β-Ti and liquid phases are included [44]. The Gibbs energy of solid solution and liquid phase are modeled with the random substitutional solution model [45]:

$$G_m^{\phi} = \sum_{i=1}^{2} X_i {}^{o}G_i^{\phi} + RT\sum_{i=1}^{2} X_i \ln X_i + X_1 X_2 L_{12}^{\phi} \tag{18}$$

where X_1 and X_2 represent the mole fractions of Ni and Ti, respectively. ${}^{o}G_i^{\phi}$ is the Gibbs energy of the element i in the structural state ϕ. L_{12}^{ϕ} accounts for the contribution of chemical composition on Gibbs energy, which is usually fitted with Redlich–Kister polynomial:

$$L_{12}^{\phi} = \sum_{k=1}^{n} {}^{k}L_{12}^{\phi}(X_1 - X_2)^k \tag{19}$$

The temperature dependence of ${}^{k}L_{12}^{\phi}$ is written as:

$${}^{k}L_{12}^{\phi} = {}^{k}A_{12}^{\phi} + {}^{k}B_{12}^{\phi}T \tag{20}$$

where ${}^{k}A_{12}^{\phi}$ and ${}^{k}B_{12}^{\phi}$ are the coefficients related to the material properties.

The compound-energy formalism (CEF) is applied to calculate the Gibbs energy of compound phases [45]. For Ni-Ti system, two-sublattice model $(A,B)_{s_1}(C,D)_{s_2}$ is applied for NiTi, Ni3Ti and NiTi2 phases, where the subscripts s_1 and s_2 are the site numbers of two sublattices, A and B are the compositions (e.g. metal element or vacancy) on the first sublattice and C and D are the compositions on the second sublattice. The Gibbs energy for the compound phase is given as:

$$\begin{aligned} G_m^{\phi} = {} & y_A^1 y_C^2 {}^{o}G_{A:C}^{\phi} + y_A^1 y_D^2 {}^{o}G_{A:D}^{\phi} + y_B^1 y_C^2 {}^{o}G_{B:C}^{\phi} + y_B^1 y_D^2 {}^{o}G_{B:D}^{\phi} \\ & + RT[s_1(y_A^1 \ln y_A^1 + y_B^1 \ln y_B^1) + s_2(y_C^2 \ln y_C^2 + y_D^2 \ln y_D^2)] \\ & + y_A^1 y_B^1(y_C^2 L_{A,B:C}^{\phi} + y_D^2 L_{A,B:D}^{\phi}) + y_C^2 y_D^2(y_A^1 L_{A:C,D}^{\phi} + y_D^2 L_{B:C,D}^{\phi}) \end{aligned} \tag{21}$$

where ${}^{o}G_{A:C}^{\phi}$ is the Gibbs energy of the compound $A_{s_1}C_{s_2}$ in the structural state ϕ. y_A^1 is the site fraction of A on the first sublattice. $L_{A,B:C}^{\phi}$ is the excess Gibbs energy arising from interactions between A and B on the first sublattice when the second sublattice is only occupied by C. The meanings of other variables in Eq. (21) are similar to those explained above. In this study, Ni3Ti, NiTi and NiTi2 are modeled as $(Ni,Ti)_{0.75}(Ni,Ti)_{0.25}$, $(Ni,Va)_{0.5}(Ni,Ti)_{0.5}$ and $(Ni)_{0.33}(Ti)_{0.67}$ respectively, where Va represents the vaccancy defect. The phase fraction and $G(\vec{X},T)$ are then calculated based on the minimal Gibbs energy principle, and other thermophysical properties, such as $H(X_1,T)$, can be calculated based on the phase fraction and $G(\vec{X},T)$.

2.4. Experiment and simulation setup

The NiTi powder (from Avimetal Powder Metallurgy Technology Ltd) and Ti powder (from Jiangsu Weilali New Material Technology Ltd) are produced with gas atomization technique. The diameters of both powders range from 20 μm (D10) to 50 μm (D90) with the median diameter around 35 μm (D50). The LPBF samples are built with a BLT-A160 LPBF machine. The wavelength of the Gaussian profile beam is around 1060 nm. To ensure that the single-track results can represent the actual processing condition, the powder layer thickness is set as 70 μm, which is around twice of the nominal powder layer thickness in typical LPBF process (suppose the apparent densities of powder layers are around 50% of their bulk densities). The element distribution in the melt tracks is characterized by energy-dispersive X-ray spectroscopy (Oxford X-Max) and electron probe microanalysis (JXA8230, JEOL).

The powder layer in the simulation is generated by modeling a rake being pushed over a powder bed using the DEM method [22]. The mesh cells in the computational domain is shown in Fig. 2. The structural Eulerian meshes with the sizes of 6 μm are adopted in the fine mesh region to capture the major physical phenomena, where X, Y and Z represent the scan, transverse and build directions respectively. Coarse meshes are extended from the fine-mesh region along X, Y, and Z directions to ensure that the vapor jet can smoothly flow out of the computational domain without abnormal wave reflection. The computation time for a simulation case with 4 million meshes and 2 ms physical time is about 7 days on a desktop with an Intel i9-12900K CPU. The material properties and numerical schemes of simulations are provided in supplementary materials.

In the practical manufacturing process, a laminar inert gas flow over the build plate (i.e., cross-flow) is usually applied to remove the by-products. The speed of cross-flow is usually around 1–2 m/s, which is much smaller than the velocity of gas flow in the fine mesh region of simulation domain (Fig. 3a1–a2). Therefore, the particle motion near the melt pool is barely influenced by the cross-flow. The experimental studies also demonstrated that the powder spattering and entrainment near the melt pool are quite similar under different flow rates of cross-flow [17,46]. The cross-flow plays an important role only when the spatters re-entry the cross-flow stream in the free-falling stage [17,46,47]. In other words, the cross-flow mainly determines the positions of redeposited spatters on the building plate. Since the present work mainly focuses on mechanisms of defect formation, here we ignore the cross-flow in the simulations. Future studies can incorporate the cross-flow in the simulation without additional technique issue.

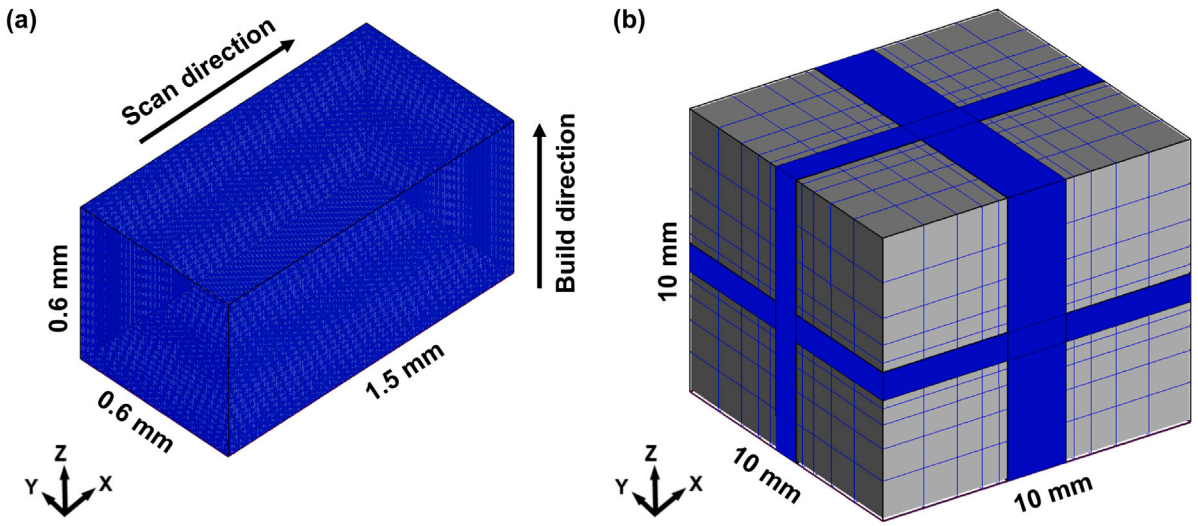

Fig. 2. Schematic diagram of computational domain and mesh. (a) Fine mesh region with the mesh size of 6 μm. (b) Entire computational domain, including the fine meshes and surrounding coarse meshes. The mesh lines are marked by blue lines. (For interpretation of the references to color in this figure legend, the reader is referred to the web version of this article.)

3. Result and discussion

3.1. Gas and particle dynamics in the melting process

Fig. 3a series show the melt pool, gas and particle dynamics during LPBF of 316L stainless steel. The vaporized metals form a high-speed and high-temperature vapor jet. Meanwhile, the pressure drop inside the vapor jet pushes the ambient gas to move toward the vapor jet region (Fig. 3a1–a2). The difference of gas flow fields under different processing parameters is mainly determined by the geometry and temperature distribution of depression zone (i.e., the cavity in the melt pool induced by the recoil pressure). For example, the laser beam is incident on the front wall of depression zone under the scan speed of 1.0 m/s, as shown in Fig. 3b1. This causes the laser energy to accumulate on the front wall of depression zone and thus produces the backward vapor ejection. As the scan speed decreases to 0.1 m/s, the laser beam is incident on the bottom and rear walls of the depression zone, causing the forward ejection of vapor shown in Fig. 3b2. The change of vapor jet direction and energy accumulation position with scan speed is also observed by the in-situ optical imaging and melt pool simulations in the previous studies [11,12]. We should note that the vapor jet direction described above is the statistical average over a time period (around 1 ms), but not the transient behavior. The gas flow field in multi-track scanning is similar with that in single-track scanning, except that the vapor jet is deviated from XZ plane due to the overlap between adjacent melt tracks.

The particle flow field is similar with the gas flow field. As shown in Fig. 3a3, the particles close to the vapor jet are rapidly blown away to form spatters, while those far from the vapor jet tend to be entrained to the vapor jet region. For multi-track scanning, the particle flow is similar with that in single-track scanning, except that the particles can only be entrained from one side of the melt track. The vapor and particle dynamics in simulations are consistent with the high-speed schlieren imaging results under the same processing conditions (no cross-flow), as shown in Fig. 3b and c series, which demonstrate the accuracy of our simulation model. More details about the simulation results are show in the supplementary videos. The velocities of spatters and entrained particles are around 4–12 m/s and 0–2 m/s respectively, which also agrees well with in-situ experiment measurements [12].

3.2. Defects induced by powder spattering

The large agglomeration induced by hot spatter coalescence can probably induce lack-of-fusion and porosity defects. Hot spatters (i.e., spatter with temperature higher than liquidus temperature) mainly originate from the melted powder particles during the melting process. As shown by the dashed circles in Fig. 4a series, when the powder particles are entrained to the vapor jet region, they are rapidly heated up from around 500 K to the liquidus temperature within 100 μs. The melted particles are then blown up by the high-speed vapor jet and become hot spatters (Type I). Some of the melted particles (particle 1 and 2 in Fig. 4b1–b2) merge with the head of melt pool and form a liquid protrusion. The liquid protrusion then breaks up into several hot spatters by the impact of high-speed vapor flow, as shown in Fig. 4b3–b5 (Type II). In addition, the melt pool fluctuation can produce hot spatters. As marked by the red circles in Fig. 4c series, the vapor jet blows up the liquid at the rear wall of the depression zone to form liquid protrusion. When the kinetic energy of liquid protrusion is large enough to overcome the surface tension force, the liquid protrusion can escape the melt pool and become hot spatters (Type III). Such kind of hot spatter is also observed in the high-speed X-ray imaging experiments [48]. According to the simulation results, around 70% of hot spatters belongs to Type I, 20% of hot spatters belongs to Type II and 10% of hot spatters belongs to Type III.

The hot spatters can further coalesce to form large agglomerations. As marked by the black dashed circles in Fig. 5a1–a2, the hot spatter at the top is pushed downward by recoil pressure to merge with an upward hot spatter and form a hot agglomeration. The hot agglomeration is then blown up and coalesce with other airborne hot spatters, which increases the size to around 100 μm (Fig. 5a3–a5). The ultra-fast X-ray images also captured the hot agglomeration induced by the coalescence of hot spatters (Fig. 5d1–d3). The size of hot agglomeration further increases after it falls on the powder bed. As shown in Fig. 5b series, when the hot agglomeration falls on the powder bed, several powder particles are bound with the hot agglomeration through the wetting effect, causing a deposited agglomeration with satellite shape. The high-speed optical images shown in Fig. 5e1–e2 also capture the formation of deposited agglomeration when the hot agglomeration falls on the powder bed. In subsequent melting process, the deposited agglomeration can be remelted and blown away to become hot spatters again, as shown in Fig. 5c series. The continuous coalescence of hot spatters can produce the agglomeration tens of times larger than the raw powder. For example, the diameter of agglomeration shown in

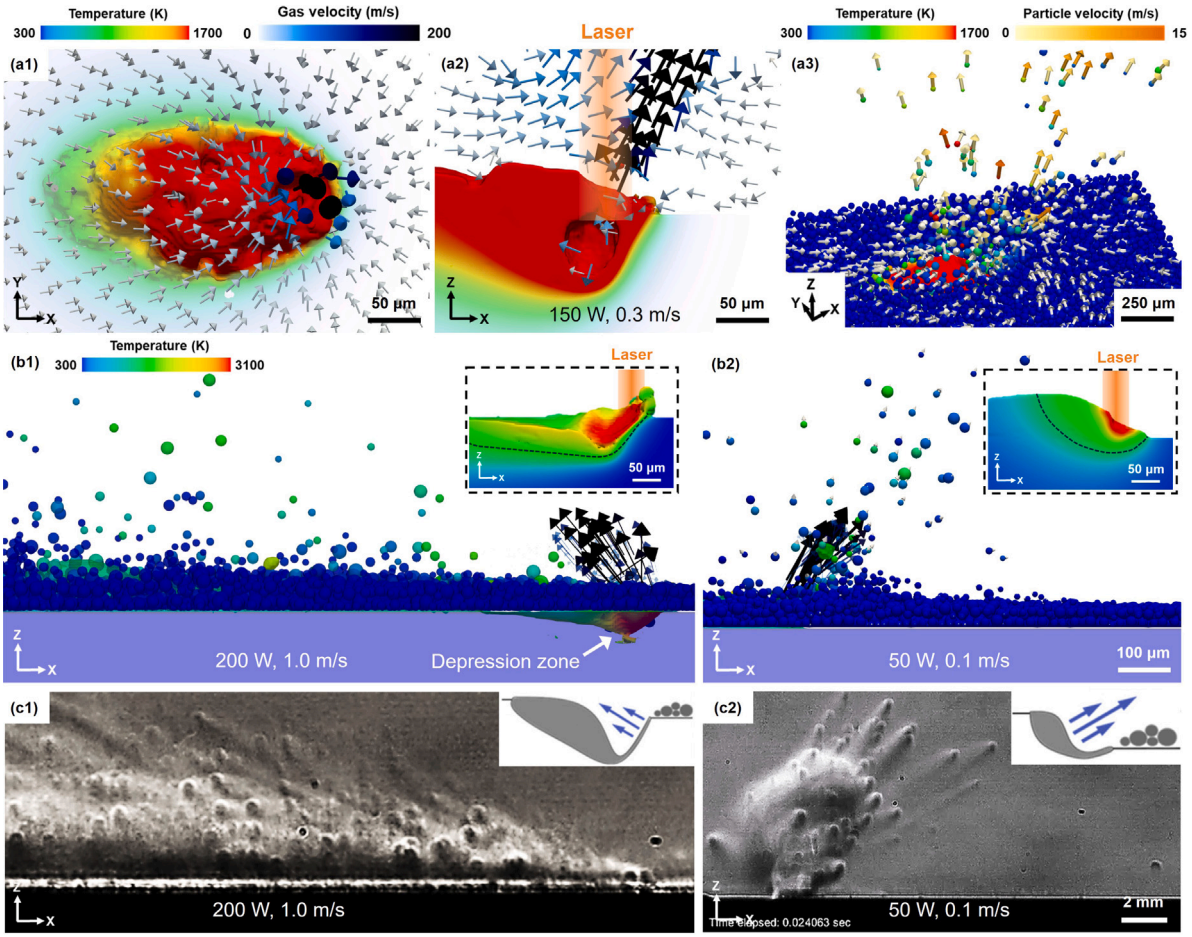

Fig. 3. Multiphase flow in the melting process. (a) Gas, melt pool and particle flow. The laser power is 150 W, scan speed is 0.3 m/s and laser diameter is 80 μm. (a1–a2) show the top and side views of gas and melt pool flow, respectively. The powder particles are hidden for better visualization. (a3) shows the temperature and velocity fields of powder particle. (b) Multiphase flow in simulations under different processing parameters. (b1) The laser power is 200 W, scan speed is 1.0 m/s and laser diameter is 50 μm. (b2) The laser power is 50 W, scan speed is 0.1 m/s and laser diameter is 50 μm. The pictures in the black dashed boxes show the temperature profiles of depression zones, where the black dashed lines mark the melt pool boundaries. The orange boxes mark the laser beam. (c) High-speed schlieren imaging results. The processing conditions are identical with those in (b). Pictures are reprinted with permission from [17], Copyright Elsevier (2018). The material is 316L stainless steel in all cases. In all the simulation results, the gas phase is set as transparent and only represented by velocity vectors for better visualization. (For interpretation of the references to color in this figure legend, the reader is referred to the web version of this article.)

Fig. 5e2 is around 20 times larger than the mean diameter of raw powder. Although the cross-flow system in current LPBF equipment helps to remove the airborne spatters and vapor plume, the hot spatters and resultant large agglomeration cannot be fully avoided during the melting process [46].

The number of hot spatters and large agglomerations formed in the melting process is influenced by the processing parameters. For example, increasing the input energy can generate a stronger vapor jet and heat the powder particles more rapidly, thus producing more hot spatters and large agglomerations. Reducing the scan speed increases the number of hot spatters generated per unit scanning length, which facilitates the formation of large agglomerations. The properties of powder bed also play important roles. Powder particles with smaller sizes and lower density are more easily melted and blown away to form hot spatters. This is also demonstrated by the in-situ X-ray experiments with Al6061 and TC4 powders under similar processing conditions [19, 21]. Increasing the thickness of powder bed increases the number of hot spatters and thus produces more large agglomerations.

The defect appears when the large agglomeration enters the range of laser beam. As shown in Fig. 6a series, the airborne agglomeration above the depression zone produces a shadowed region on the rear wall and part of the front wall of the depression zone (black box in Fig. 6a2). The temperature of shadowed region drastically falls below the boiling temperature, making the recoil pressure decrease to zero. The fluid at the rear wall of depression zone then moves forward and forms a forward protrusion, as marked by the black arrow in Fig. 6a2–a3. Meanwhile, a mini depression zone forms in the unshadowed region at the front wall of the depression zone (orange box in Fig. 6a2). The deepening of mini depression zone produces a backward protrusion at its left side, as marked by orange arrow in Fig. 6a2. The forward and backward protrusions continuously elongate and eventually merge to form a temporary gas pore (Fig. 6a3–a4). Due to the decrease of recoil pressure, the liquid velocity in the shadowed region is lower than that in the normal state. Moreover, the temperature drop at the surface of shadowed region decreases the thermocapillary force on the gas pore [49]. Therefore, unlike the keyhole pore caused by the overheating [18], the temporary gas pore mainly oscillates at its position of generation. After the airborne agglomeration exits the range of laser beam, the depression zone gradually recovers to the normal state (Fig. 6a5–a6). However, the temporary gas pore is captured by the solidification front and becomes a gas pore defect in the melt track (Fig. 6a6).

Similar phenomena occur when the large agglomeration is deposited on the powder bed. As shown in Fig. 6b1–b3, as the laser irradiates on the deposited agglomeration, a forward protrusion at the rear wall of depression merges with the front wall of depression and generates a large gas pore. The depression zone remains in an abnormal

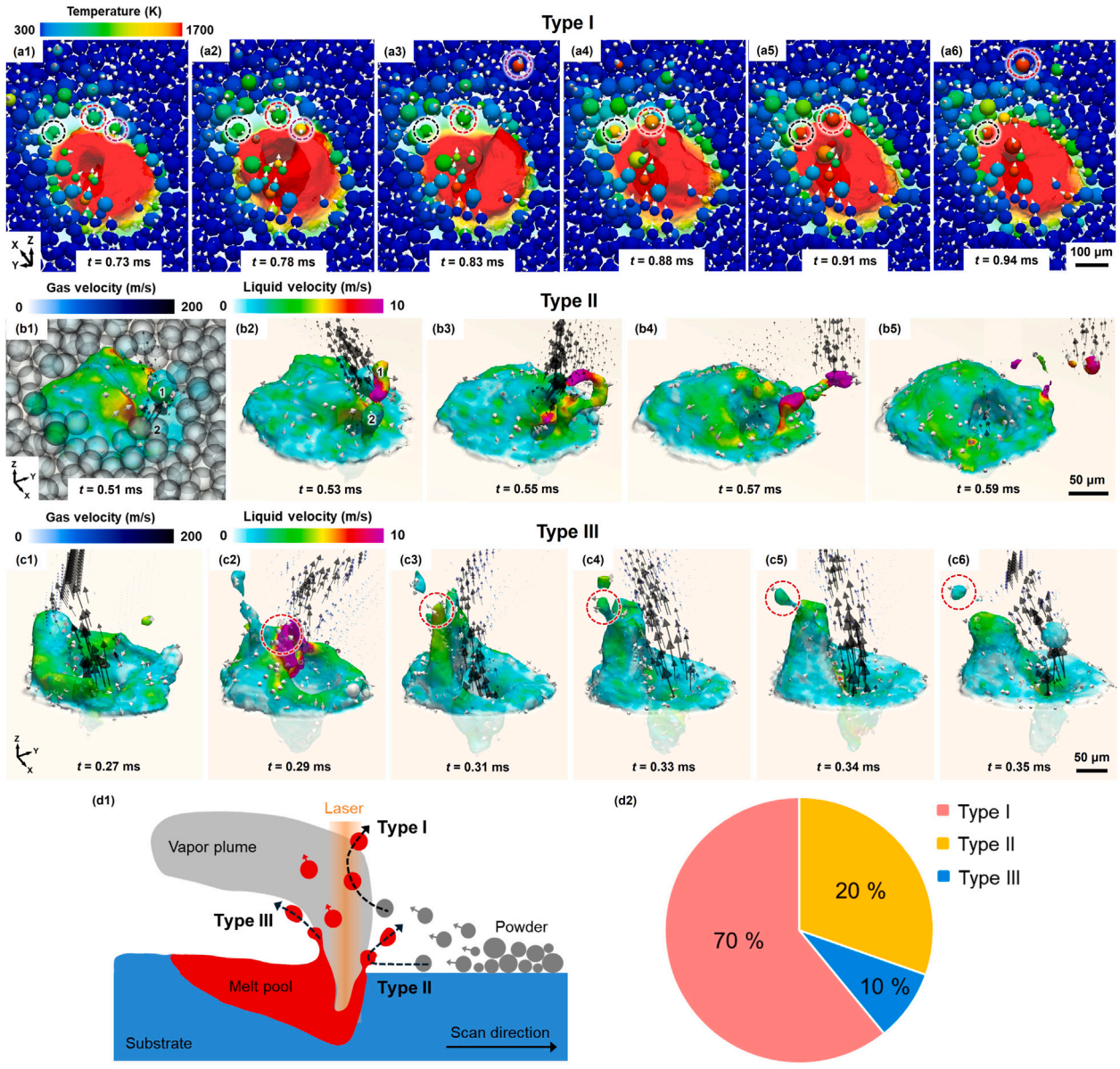

Fig. 4. Formation of hot spatters. (a) Hot spatters caused by the ejection of melted powder particles (Type I). The powder particles marked by blue, red and purple dashed circles are first entrained to the vapor jet region, then melted by laser irradiation, and finally blown away to form hot spatters. (b) Hot spatters caused by the breakage of the liquid protrusion (Type II). The melted powder particle (particle 1 and 2) merges with the head of melt pool and forms a liquid protrusion. The liquid protrusion then breaks into several hot spatters by the impact of high-speed vapor flow. (c) Hot spatters induced by the melt pool fluctuation (Type III). The liquid at the rear wall of the depression zone is blown up and ripped by the vapor flow, causing hot spatters. (d1) Schematic diagram of three types of hot spatters. The black dashed lines mark the formation trajectories of hot spatters. (d2) The proportions of three types of hot spatters. The powder particles in (b2–b5) and (c) series are hidden for better visualization. The laser power is 150 W, scan speed is 0.3 m/s, laser diameter is 80 μm and material is 316L stainless steel in all simulation cases. (For interpretation of the references to color in this figure legend, the reader is referred to the web version of this article.)

state when the liquid around the gas pore solidifies, causing a gas pore defect in the melt track (Fig. 6b4–b5).

The geometry of gas pore defect is affected by the processing parameters. Fig. 6c series show the formation of an irregular gas pore defect under the scan speed of 0.8 m/s. As the agglomeration enters the range of laser beam, the front and back walls of depression zone start to collapse (Fig. 6c1–c2). However, due to the higher solidification rate under the large scan speed, the liquid near the depression zone starts to solidify when the depth of depression zone decreases to around half of the normal value (Fig. 6c3–c5). This causes an irregular V-shape pit at the position where the depression zone collapses. The irregular V-shape pit cannot be fully filled with liquid during the recovery of depression zone, which finally causes an irregular gas pore defect (Fig. 6c6). When the scan speed further increases to 1.2 m/s, as shown in Fig. 6d, the laser beam is mainly incident on the front wall of depression zone. As the large agglomeration enters the laser beam, a mini depression zone forms at the front wall of depression zone and produces a backward protrusion, which is similar with the situation in Fig. 6a. As the depth of mini depression increases, the protrusion merges with the back wall of depression zone and causes an irregular gas pore (Fig. 6d2–d4). Moreover, the tail of melt pool rapidly solidifies and forms a shallow pit at the surface of melt track (Fig. 6d4), which increases the surface roughness at the top surface.

However, not all agglomerations induce defects. Fig. 7a shows the formation of defect-free melt track under the influence of large agglomeration. The processing parameters are identical with those in Fig. 6a, except that the diameter of agglomeration decreases from 150 μm to 100 μm. The formation process of temporary gas pore (Fig. 7a1–a3) is

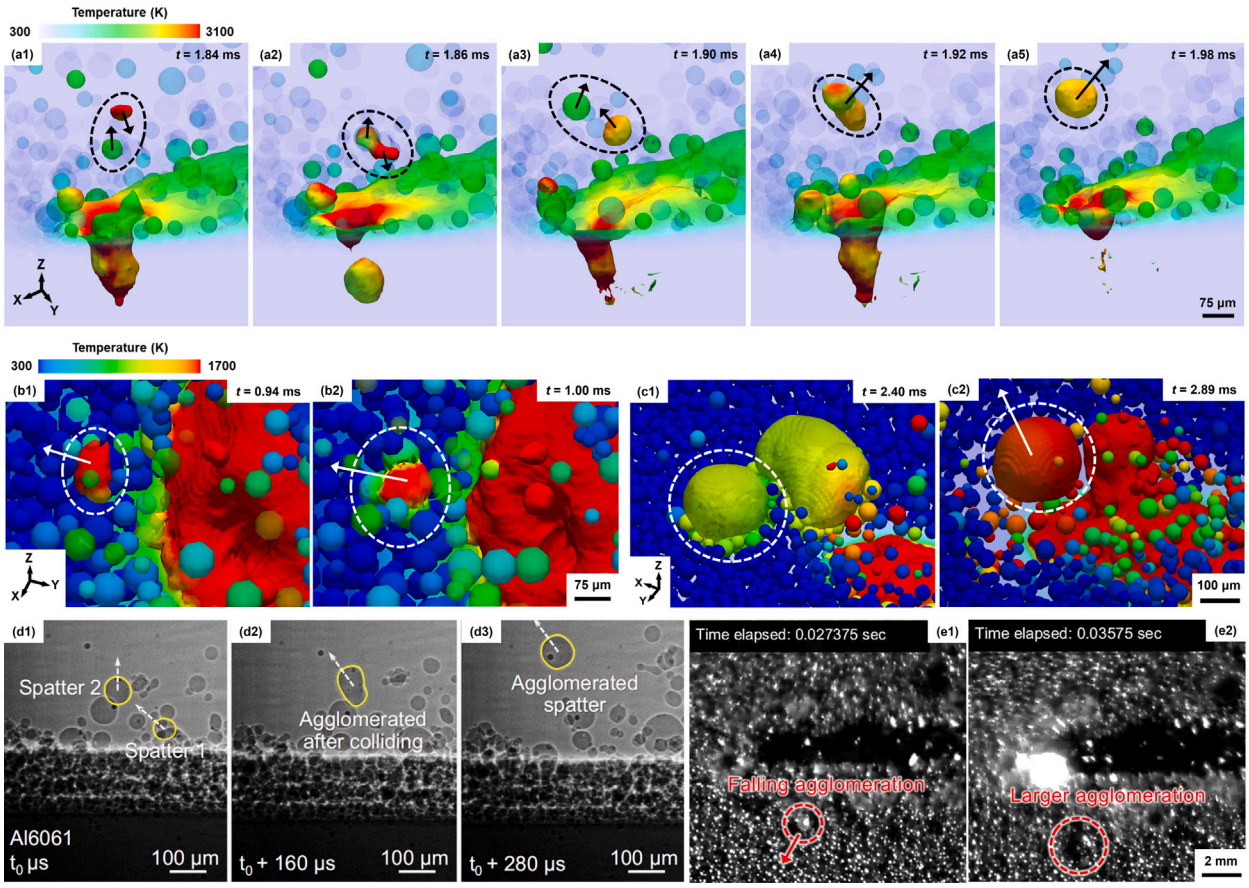

Fig. 5. Large agglomeration formed by the coalescence of hot spatters. (a) Coalescence of airborne hot spatters to form hot agglomeration. The black arrows mark the velocities of airborne hot spatters and hot agglomeration. (b) Coalescence of fallen hot agglomeration and powder particles to form deposited agglomeration. The white arrows mark the velocities of hot agglomeration. (c) Melting and ejection of deposited agglomeration. The laser power is 150 W, scan speed is 0.3 m/s, laser diameter is 80 μm and material is 316L stainless steel in all simulation cases. (d) Coalescence of airborne hot spatters during the melting of Al6061. The ultra-fast X-ray images are reprinted with permission from [19], Copyright Nature Portfolio (2022). (e) Coalescence of fallen hot agglomeration and powder particles during the melting of 316L stainless steel. The high-speed optical images are reprinted with permission from [17], Copyright Elsevier (2018). (For interpretation of the references to color in this figure legend, the reader is referred to the web version of this article.)

similar with that in the case with 150 μm agglomeration (Fig. 6a1–a3). However, the agglomeration is blown away from the range of laser beam only 0.04 ms after the formation of temporary gas pore (Fig. 7a4–a5), which is much faster than that in the case with 150 μm agglomeration (Fig. 6a4–a5). This causes the position of temporary gas pore to be closer to the position where the depression zone recovers. During the recovery of depression zone, the depth of depression zone keeps increasing, which gradually pushes away the liquid at the top of temporary gas pore. Meanwhile, the temperature increase at the surface of depression zone increases the thermocapillary force on the gas pore, which pushes the gas pore to the surface of depression zone. The two factors drives the temporary gas pore to contact and merge with the depression zone, forming a depression zone with unstable surface (Fig. 7a5). The laser rays are then incident on the bottom of newly formed depression zone and rapidly increases the recoil pressure. This helps to avoid the re-collapse of newly formed depression zone and gradually shape it into the normal state (Fig. 7a6). In this way, the temporary gas pore is fully eliminated by the timely recovery of depression zone. Through analyzing the elimination of temporary gas pore under different processing parameters, we find that criterion of defect generation is:

$$L < L_c \tag{22}$$

where L is the distance between the positions where the depression zone collapses and where it recovers, as shown in Fig. 7b. Note that the position of the temporary defect is very close to the position where the depression zone collapses. L_c is the critical distance, which is constant under specific processing parameters and material. When $L < L_c$, the temporary gas pore is close enough to the position where the depression zone recovers. That means the temporary gas pore can merge with the depression zone during the recovery of depression zone and the newly formed depression zone can be quickly stabilized by recoil pressure. In this way, the temporary gas pore can be fully eliminated, as shown in Fig. 7b1. When $L > L_c$, either the temporary gas pore fails to merge with the depression zone or the newly formed depression zone re-collapses, both of which lead to the gas pore defect in the solidified region (Fig. 7b2). If the melting mode is stable keyhole mode (usually regarded as the optimal melting mode [50]), L_c is close to the size of temporary gas pore:

$$L_c = \min(D_d, D_l) \tag{23}$$

where D_l is the laser diameter and D_d is the diameter of depression zone at the half depth of depression zone, as shown in Fig. 7b. Eq. (22) can be applied to identify the position of defect caused by large agglomeration. Since L and L_c are hard to measure by experimental methods, here we define another two variables τ and τ_c that are relatively easy to measure:

$$\tau = \frac{L}{V}, \quad \tau_c = \frac{L_c}{V} \tag{24}$$

where V is the scan speed. τ represents the time duration of large agglomeration that causes the shadowed region in the depression zone, which is very close to the time duration of large agglomeration inside

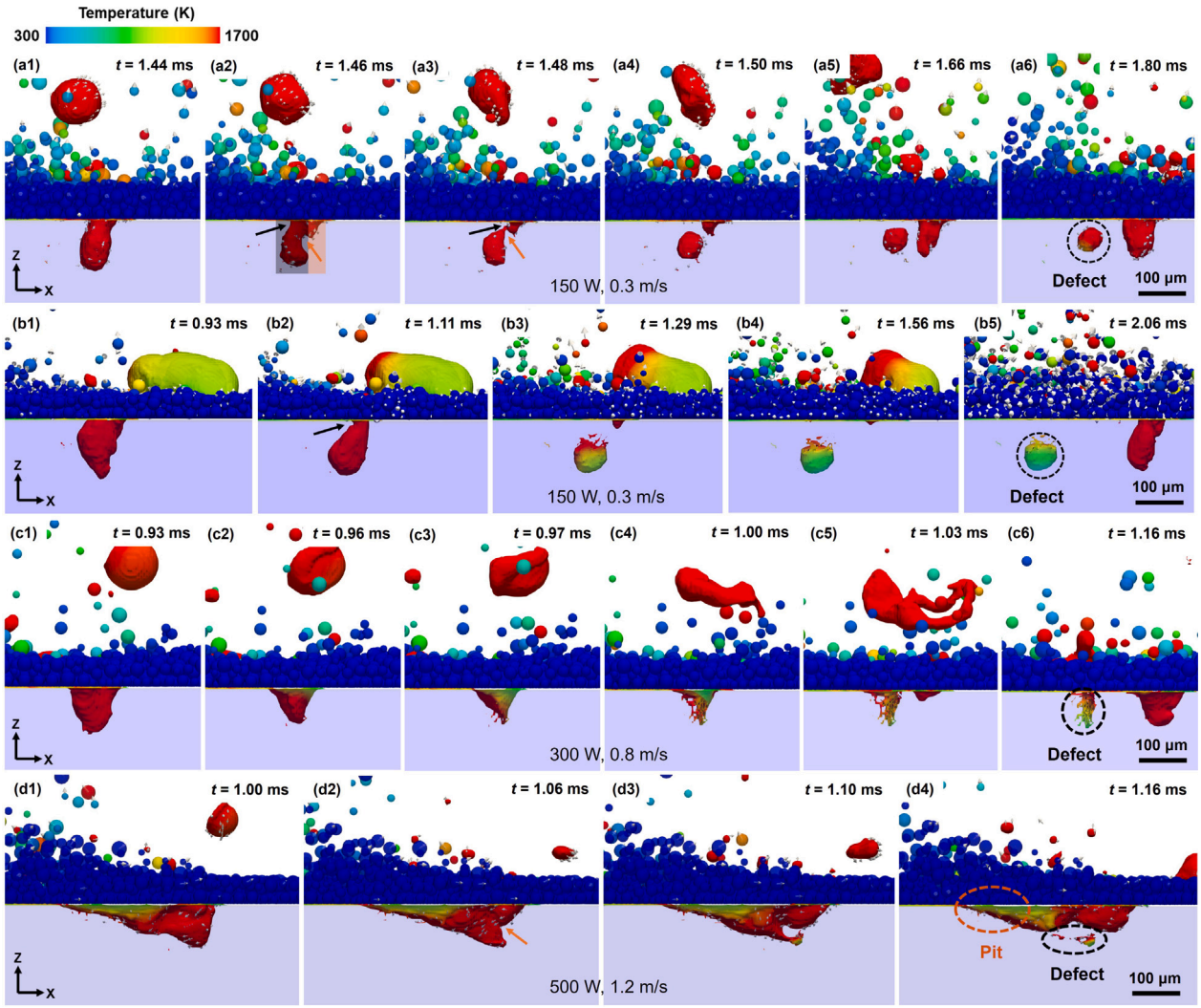

Fig. 6. Defects induced by large agglomerations. (a) Gas pore defect caused by the airborne agglomeration. The black and orange boxes mark the shadowed and unshadowed regions induced by the airborne agglomeration, respectively. The black and orange arrows mark the forward and backward protrusions at the rear and front walls of the depression zone, respectively. The laser power is 150 W and scan speed is 0.3 m/s. (b) Gas pore defect caused by the deposited agglomeration. The black arrow marks the forward protrusion at the rear wall of the depression. The laser power is 150 W and scan speed is 0.3 m/s. (c) Irregular gas pore defect caused by the airborne agglomeration. The laser power is 300 W and scan speed is 0.8 m/s. (d) Gas pore and pit caused by the airborne agglomeration. The laser power is 500 W and scan speed is 1.2 m/s. The laser diameter is 80 μm and material is 316L stainless steel in all cases. (For interpretation of the references to color in this figure legend, the reader is referred to the web version of this article.)

the range of laser beam. τ_c is constant under specific material and processing parameters. In this way, Eq. (22) can be rewritten as:

$$\tau < \tau_c \tag{25}$$

By recording τ and comparing τ with τ_c, we can detect the position of defects induced by the large agglomeration in the printed part.

To better understand the criterion of defect generation (Eq. (25)), we further perform simulations with large agglomerations under different processing parameters. The melting mode is stable keyhole mode in all simulation cases. As shown in Fig. 7c1, D_d is smaller than D_l when the scan speed is smaller than 1.0 m/s. As the scan speed further increases to 1.2 m/s, D_d gradually increases above D_l. Fig. 7c2 show the results of τ_c under different V. As V increases from 0.3 m/s to 1.2 m/s, τ_c decreases from 157 μs to 67 μs. This indicates that the defect induced by large agglomeration is more likely to occur under larger scan speed.

Fig. 7b3 shows the lowest size of agglomeration that can induce defects. When V increases from 0.3 m/s to 1.2 m/s, the critical size of agglomeration decreases from 120 μm to 80 μs. This explains why LPBF parts can still achieve high relative density (> 99.99%) when numerous spatters are generated in the printing process, since the sizes of most spatters are close to the size of raw powder. We should note that the results in Fig. 7c3 are obtained from simulations with only one agglomeration in the range of laser beam. If multiple agglomerations are simultaneously inside the range of laser beam, the lowest size of agglomeration may further decrease. In this case, it is better to apply Eq. (25) to judge the occurrence of defects.

In addition to the size of agglomeration, τ is also related to the velocity of agglomeration. The simulation results show that the agglomeration is more likely to induce defects when it enters the laser beam along the scan direction with the speed around 1–2 m/s. Take the simulation with $V = 0.3$ m/s for example, the agglomeration of 130 μm in diameter and 1.5 m/s in velocity can induce porosity defect in the melt track, while the agglomeration of 160 μm in diameter and 0.3 m/s in velocity is blown away by the vapor jet without causing defect.

The formation mechanism of lack-of-fusion defect is similar with that of gas pore defect. Under the processing parameters in Fig. 6, the melting mode of melt pool changes from stable keyhole mode to the conduction mode when the large agglomeration is inside the range of laser beam. If the size of agglomeration is larger than that in Fig. 6, the energy absorbed by the powder bed and substrate is insufficient to form conduction melting mode when the large agglomeration is in the range

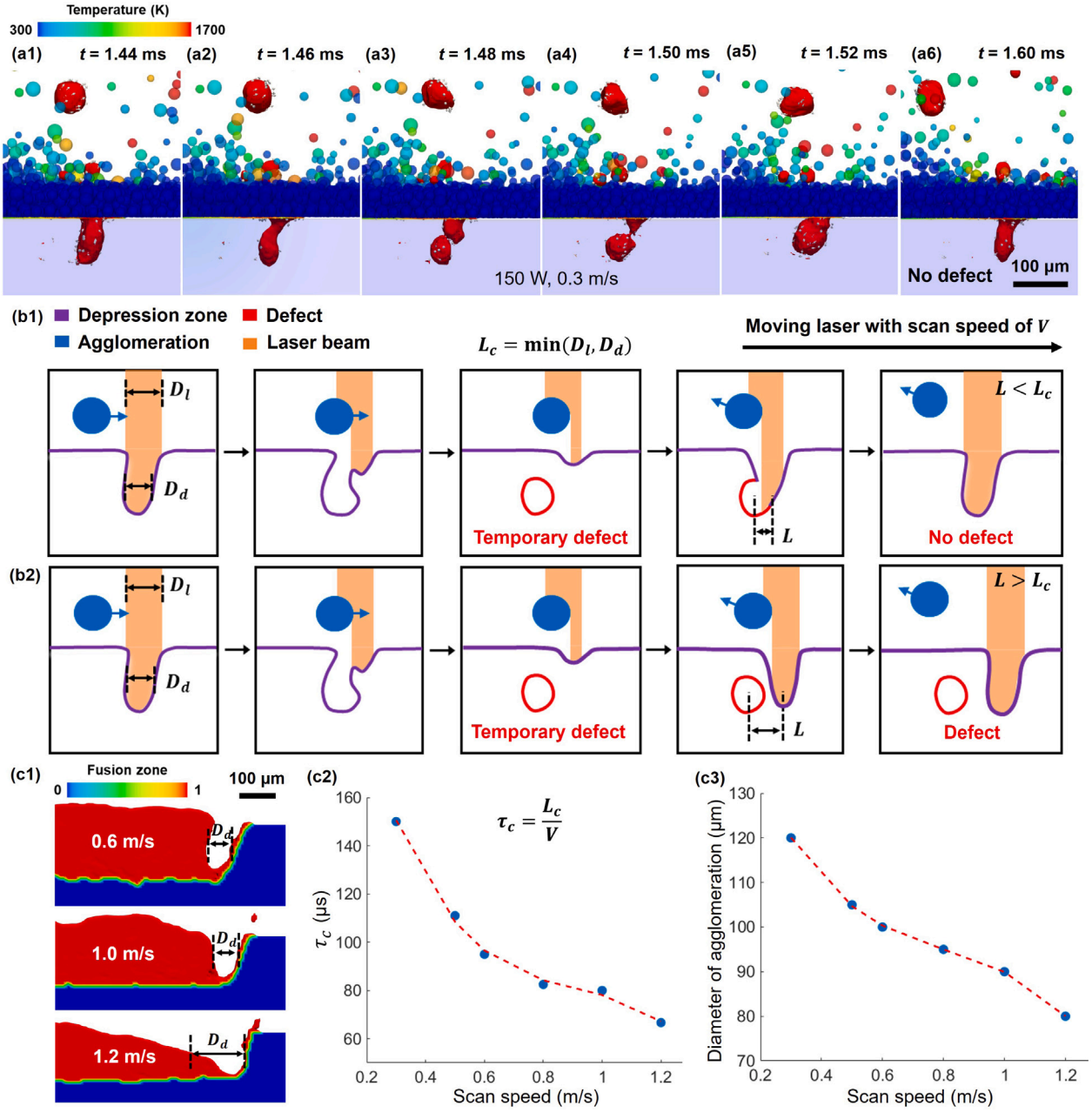

Fig. 7. Criterion of defect generation induced by large agglomeration. (a) Defect-free melt track under the influence of large agglomeration. The processing parameters are identical with those in Fig. 6a, except that the size of agglomeration decreases to 100 μm. (b) Schematic diagrams of defect generation criterion. (b1) When $L < L_c$, the position of temporary defect is close to the position where the depression zone recovers. In this way, the temporary defect can be eliminated by the recovery of depression zone. (b2) When $L > L_c$, the position of temporary defect is far from the position where the depression zone recovers, leading to the defect in the solidified region. (c) Influence of scan speed and agglomeration size on defect formation. The melting mode is stable keyhole mode, laser diameter is 80 μm and material is 316L stainless steel in all simulation cases. (c1) The morphology of depression zone under different scan speeds. (c2) τ_c under different scan speeds. (c3) The lowest size of agglomeration that can induce defects under different scan speeds.

of laser beam. This leads to not only the gas pore defect at the position where depression zone collapses, but also the lack-of-fusion defect at the position where the melt pool is in abnormal state. Similarly, if the energy input is smaller than that in Fig. 6, the powder bed on the substrate may not be fully melted when the large agglomeration is in the range of laser beam, causing lack-of-fusion defect. The size of lack-of-fusion defect is close to L, which can be much larger than the size of gas pore caused by the collapse of depression zone. Such lack-of-fusion defects can also be found in the simulation with pre-sintered powder bed [27].

The laser irradiation on the large agglomeration also increases the probability of defect generation in other places of build plate, causing the "chain reaction" of defects. As shown in Fig. 8a, the airborne agglomeration splits into several liquid droplets when the recoil pressure on the agglomeration is large enough. These droplets may further coalesce with other particles to form large agglomeration and induce defects in subsequent melting process. In addition to the split of agglomeration, the laser-agglomeration interactions can disturb the surrounding powder bed, which increases the probability of defect generation in adjacent melt tracks. As shown in Fig. 8b series, during the laser-agglomeration interaction, the vapor is horizontally ejected from the side of deposited agglomeration and sweeps away the surrounding powder particles (red boxes in Fig. 8b2–b3). The abnormal vapor jet decreases the layer thickness near the melt track to zero, and increases the layer thickness away from the melt track. This may not only increase the surface roughness of printed part but

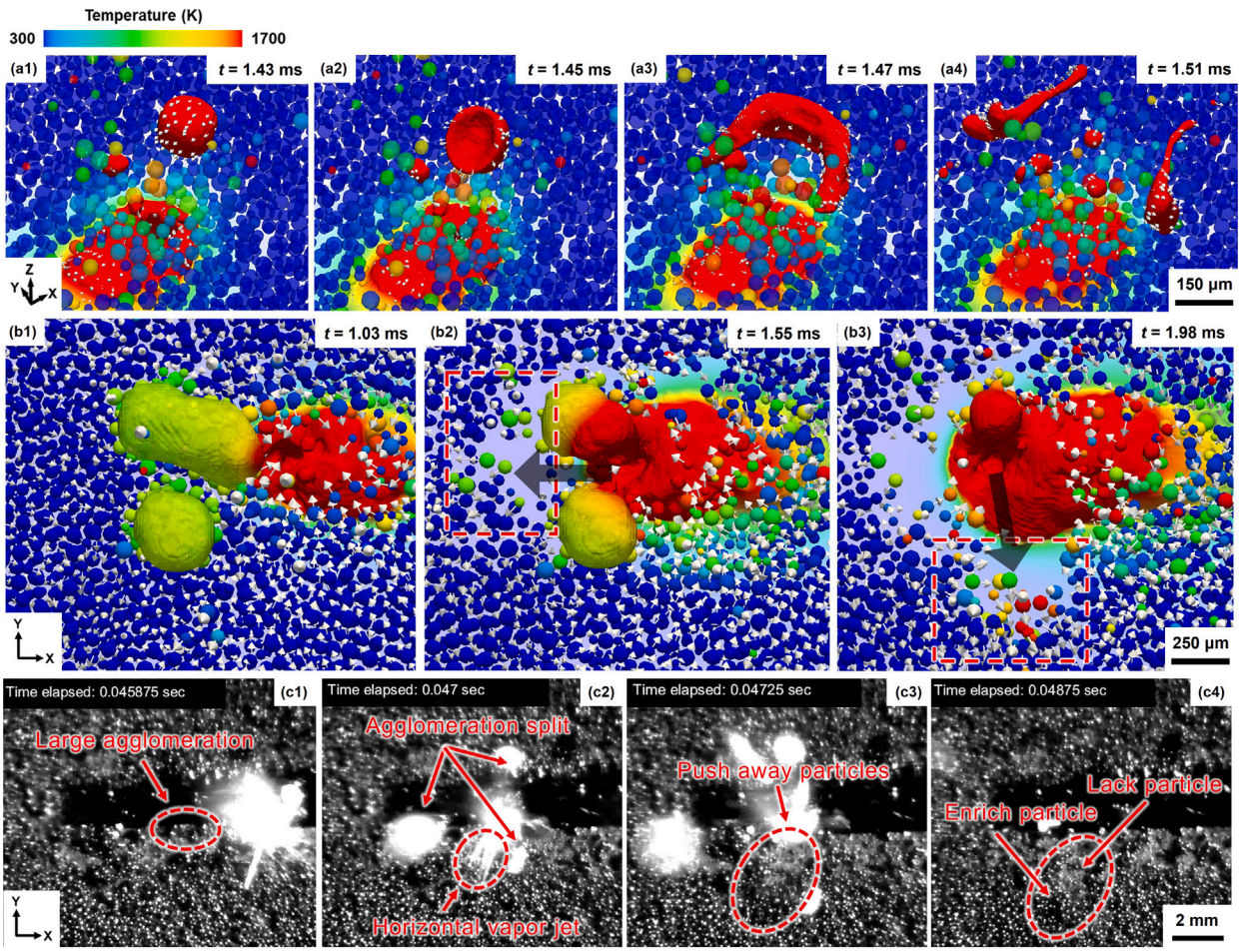

Fig. 8. "Chain reaction" of defects induced by large agglomerations. (a) Splitting of a large agglomeration into several liquid droplets under laser irradiation. (b) Degradation of powder bed quality during the laser irradiation on agglomeration. The black large arrows mark the directions of horizontal vapor jets. The red boxes show the lack-particle region induced by horizontal vapor ejection from the side of agglomeration. The laser power is 150 W, scan speed is 0.3 m/s, laser diameter is 60 μm and material is 316 stainless steel in all simulation cases. (c) Splitting of large agglomerations and degradation of powder bed quality in high-speed optical images. Pictures are reprinted with permission from [17], Copyright Elsevier (2018). (For interpretation of the references to color in this figure legend, the reader is referred to the web version of this article.)

also cause defects in adjacent tracks. For example, when the laser beam enters or exits the lack-particle/enrich-particle regions on the powder bed, the laser irradiation on depression zone suddenly changes, which can intensify the melt pool fluctuation and produce gas pore defects. Moreover, the melting of rich-particle region can produce more hot spatters and increase the probability of large agglomeration formation. The high-speed optical images also validate the simulation prediction. As shown in Fig. 8c1–c2, the large agglomeration splits into several hot spatters during the laser irradiation process. Meanwhile, the horizontal vapor jet pushes away the surrounding particles to form lack-particle and enrich-particle regions on the powder bed (Fig. 8c2–c4).

3.3. Defects induced by powder entrainment

The entrainment of powder particles to the melt pool can also introduce defects to the printed part. Fig. 9a series show the entrainment of powder particles to the melt pool during LPBF of TC4 material. When the entrained particles contact the melt pool surface, the melt starts to wet the surfaces of particles and drag the particles into the melt pool ($\theta_e \approx 20°$ [37,51]). Meanwhile, these particles are rapidly heated by the surrounding melt. As shown by particle 2 in Fig. 9a1–a3, the particle is fully melted when half of the particle is wetted by the melt. The melted particle then dissolves in the melt pool through the melt pool convection (Fig. 9a4–a5). Since some of the raw powder particles contain inert gas pores (especially for powder produced by gas atomization), the dissolution of entrained particles can introduce the inert gas pores to the melt pool. If the melt around the entrained particle solidifies before the particle is fully melted, like particle 1 in Fig. 9a series, the particle is decelerated by the solidifying melt and finally adheres to the surface of the melt track. The results indicate that the entrained particles cannot submerge in the melt pool without melting in single-material LPBF. The speculation is also validated by the single-track single-material LPBF experiments (Ni, Fe, Ti and Al based alloys) [52–57]. This implies that the unmelted particles in the bulk samples of single-material LPBF are probably induced by large agglomerations, not particle entrainment.

However, the entrained solid particles can fully submerge in the melt pool during multi-material LPBF, causing particle inclusion defects. Fig. 9b shows the submergence of Ti particle (marked by the white dashed circle) in the melt pool during LPBF of Ti powder on a Ni substrate. The laser power is 90 W and scan speed is 0.1 m/s. When the particle contacts the melt pool surface, the temperature of particle rapidly increases to that of surrounding melt. However, since the temperature of melt near the particle is lower than the liquidus temperature of Ti (1928 K), the particle is still in solid state when it fully submerges in the melt pool, causing particle inclusion defects after the solidification of melt pool. Experiment results also provide evidence of Ti particle inclusions in the melt track, as shown in Fig. 9c series.

The particle inclusion defect is mainly caused by the lower liquidus temperature of metallurgical products formed by the metallurgical reactions. During the melting process, the melted Ti and Ni react and

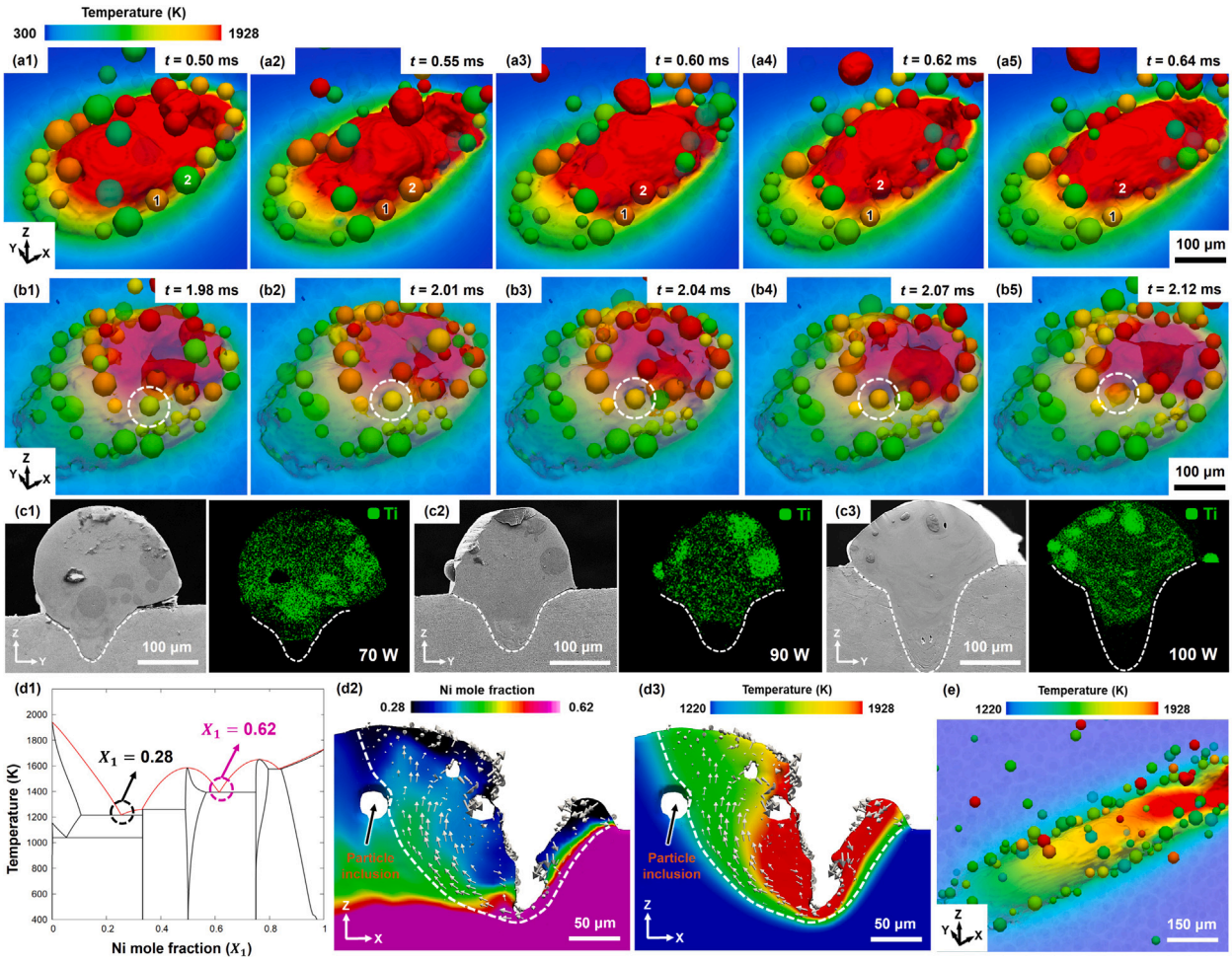

Fig. 9. Particle inclusion defects induced by powder entrainment. (a) The entrainment of TC4 particles to the melt pool in single-material LPBF. Particle 1 is not fully melted when the liquid around the particle solidifies. Particle 2 is fully melted when half of the particle is wetted by the melt pool liquid. (b) Formation of a Ti particle inclusion during the melting of Ti powder on a Ni substrate. The laser power is 90 W and scan speed is 0.1 m/s. For better visualization, the transparency of particle is increased with the decrease of temperature. (c) Experimental evidence of Ti particle inclusions in the melt track. The left and right pictures show the scanning electron microscope (SEM) and energy dispersive spectroscopy (EDS) results, respectively. (d) Formation mechanisms of particle inclusion defects. (d1) Phase diagram of Ni-Ti system. The liquidus line is marked by the red line. (d2–d3) Ni element and temperature distributions of melt pool. The processing parameters are identical with those in (b). The white dashed lines mark the melt pool boundaries. The particles are hidden for better visualization. (e) Decreasing the particle inclusion defects by increasing the scan speed. The laser power is 250 W and scan speed is 1.0 m/s. The laser diameter is 60 μm in all simulation cases. (For interpretation of the references to color in this figure legend, the reader is referred to the web version of this article.)

form the metallurgical products with different compositions in the melt pool (Fig. 9d2). Under the processing parameters in Fig. 9b, the Ni mole fractions of these products are between 0.28 to 0.62 (Fig. 9d2). According to the liquidus line in Ni-Ti phase diagram (Fig. 9d1), the liquidus temperatures of these products are lower the liquidus temperatures of Ti. That means these products can still flow in the melt pool when their temperatures are below the liquidus temperatures of Ti, as shown by the yellow and green regions in Fig. 9d3. When Ti particles contact the metallurgical products with temperatures below the liquidus temperature of Ti, Ti particles remain in solid state during the submergence (Fig. 9b). This finally causes the particle inclusion defect in the solidified region (Fig. 9d3). For single-material LPBF, the temperature of melt is always larger than the liquidus temperature of powder particles, so the particles can be fully melted before the submergence in the melt pool. The results indicate that the particle inclusion defect may occurs when the liquidus temperature of metallurgical product is lower that of powder particle:

$$T_l(\vec{X}_m) \le T_l(\vec{X}_p) \tag{26}$$

where $\vec{X}_m$ and $\vec{X}_p$ are the mole fraction vectors of metallurgical product and powder particle, respectively. Eq. (26) suggests that the particle inclusion defect may also occur in single-material LPBF when the thermophysical properties of material at the particle surface (e.g., oxidation layer) are quite different with those inside the particle.

The elimination of particle inclusion defects is mainly through the convective heat transfer between particle and melt pool liquid in the remelting process. If $T_l(\vec{X}_p)$ is slightly higher than $T_l(\vec{X}_m)$, the particle inclusions in the current melt track can be melted during the melting of adjacent melt tracks. However, if $T_l(\vec{X}_p)$ is much higher than $T_l(\vec{X}_m)$, the particle inclusion defects are difficult to fully eliminate. Take LPBF of Ti-Nb powder mixture for example, many Nb particle inclusion defects exist in the as-print sample, even when the input energy is several times larger than those for pure Nb and pre-alloyed TiNb powders [58–60]. A possible solution to mitigate particle inclusion defects is to increase the scan speed. The idea of the solution is to ensure that the melt around the particle solidifies before the particle completely submerges in the melt pool. Suppose the melting modes of melt pool are identical under different scan speeds. The solidification rate of melt increases with the increase of scan speed. On the other hand, for particles entrained to the melt pool, the time duration from contacting the melt pool surface to the complete submergence in the melt pool is relatively fixed under different scan speeds. This is because the submergence of particle is mainly governed by the wetting force, which is almost independent of

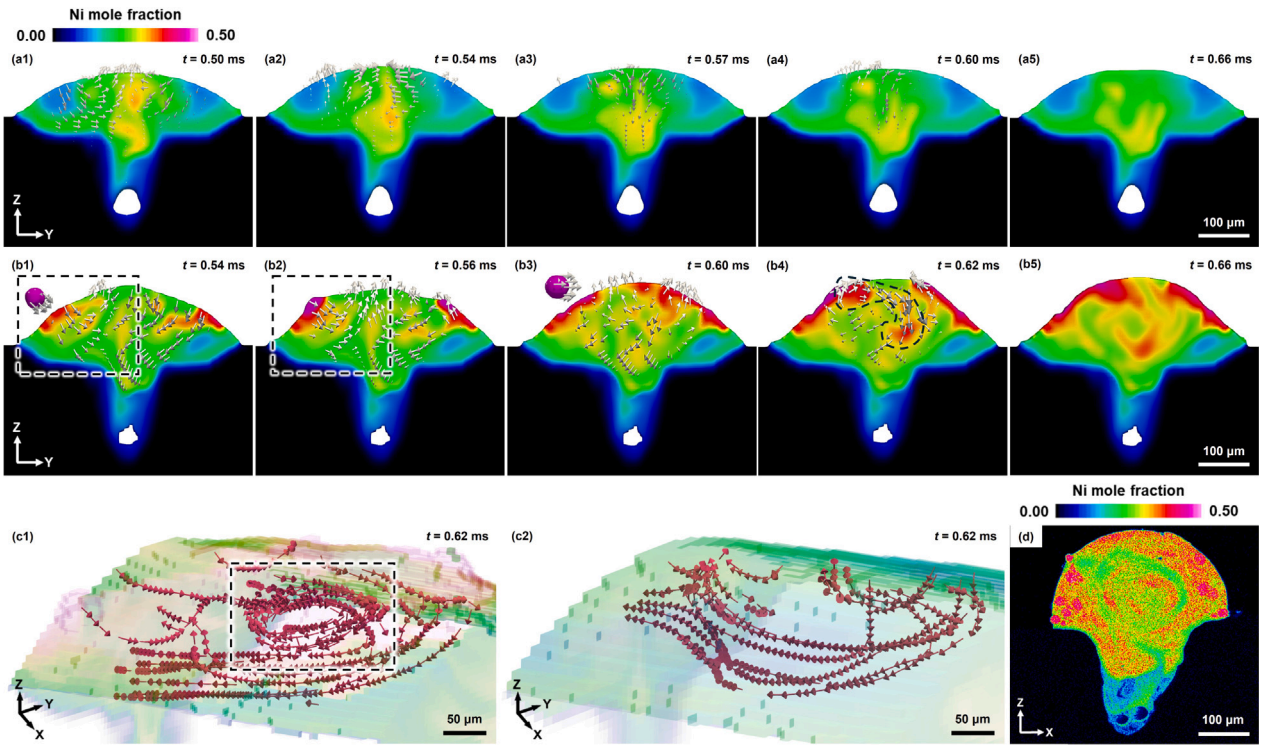

Fig. 10. The influence of entrained particles on flow field and element distribution. (a) Flow field and Ni element distribution at the melt pool tail during the melting of pre-sintered NiTi powder bed on a Ti substrate. The white arrows mark the liquid velocity. (b) Flow field and Ni element distribution at the melt pool tail during the melting of loose NiTi powder bed on a Ti substrate. The black dashed contours mark the intensified vortex flow caused by entrained particles. (c) Streamlines of liquid flow at the melt pool tail. (c1) With loose NiTi powder bed. The black dashed box marks the single vortex flow caused by the entrained particles. (c2) With pre-sintered NiTi powder bed. (d) Electron probe micro-analyzer (EPMA) result of Ni distribution in the melt track with loose NiTi powder bed. The laser power is 200 W, scan speed is 0.3 m/s and laser spot size is 90 μm in all simulation cases. (For interpretation of the references to color in this figure legend, the reader is referred to the web version of this article.)

scan speed. Therefore, entrained particles are more likely to adhere to the surface of melt track under large scan speed, rather than submerge in the melt pool (like particle 1 in Fig. 9a). The simulation results also show that the number of particle inclusion defects decreases when the scan speed increases to 1.0 m/s, as shown in Fig. 9e.

In addition to the particle inclusion defect, the entrained particle also influences the flow field at the melt pool tail. As shown in Fig. 10a series, when the pre-sintered NiTi powder bed is fused on a Ti substrate, the flow field is the typical Marangoni flow. The liquid at the melt pool surface is pushed to the edge of the melt pool while the liquid below the surface is pushed to the center of the melt pool, causing the symmetrical vortex flow shown in Fig. 10a1. However, if the powder bed is loose, the momentum of entrained particle can destroy the symmetry of vortex flow. As shown by the black boxes in Fig. 10b1–b2, when the particle with velocity of 1 m/s impacts the left part of melt pool, the momentum of particle intensifies the vortex flow at the left side. The influence is more significant when the particle impacts the region close to the solidification front. As shown in Fig. 10b3–b4, since the liquid velocity at the melt pool tail is much smaller than the velocity of particle, the flow field is changed from symmetrical vortex flow to single vortex flow under the impact of particle. 3D streamlines in Fig. 10c1 also display the single vortex flow caused by the impact of particle at the melt pool tail.

The change of flow field directly influences the element distribution at the top of melt track. When NiTi particle contacts the melt pool tail (Fig. 10b3–b4), Ni element diffuses along the streamlines of single vortex from the contact point (black dashed contour in Fig. 10b4). Since the melt pool tail is close to the solidification front, the liquid near the contact position solidifies 0.05 ms after the NiTi particle contacts the melt pool tail (Fig. 10b3–b5). This causes the single-vortex distribution of Ni element being retained at the top of the melt track (Fig. 10b5). The single-vortex distribution of Ni element is also validated against the experiment result shown in Fig. 10d. In fact, the evaporation rate of one element can be quite different at different positions of depression zones. This leads to the heterogeneous distribution of elements in single-material LPBF, especially for elements with low boiling points [61]. Therefore, the particle entrainment can also influence the element distribution in single-material LPBF.

4. Conclusions

In the present work, we have developed a CFD–DEM-CALPHAD coupling model to simultaneously elucidate the gas, melt pool and particle dynamics in single- and multi-material LPBF process. Our model is validated against the experiments with different materials and processing parameters. Through the high-fidelity simulation, we successfully uncover the formation mechanisms of defect caused by powder spattering and entrainment. The main conclusions are as follows:

(1) The large agglomeration formed by hot spatter coalescence can probably induce lack-of-fusion and gas pore defects in LPBF parts. The hot spatters mainly originate from the melted powder particles near the vapor jet region. These hot spatters then coalesce with other particles to form large agglomerations. As the large agglomeration enters the range of laser beam, the depression zone collapses and forms gas pores. Meanwhile, the powder bed on the substrate may not be fully melted after the collapse of depression zone, causing lack-of-fusion. If the time duration of agglomeration inside in the range of laser beam is larger than a critical value, the temporary defect are retained in the melt track and become defects.

(2) The powder entrainment can probably cause particle inclusion defects in multi-material LPBF. In single-material LPBF, the temperature of melt is larger than the liquidus temperature of powder particles, so the entrained particles can be fully melted before the submergence in

the melt pool. In multi-material LPBF, however, the temperature of melt can be lower than the liquidus temperature of powder particles due to the metallurgical reactions among different feedstocks. This enables the powder particles to submerge in the melt pool without melting, causing particle inclusion defects. In addition, the powder entrainment can alter the flow field at the melt pool tail. When the powder entrainment is not symmetrical at the melt pool tail, the momentum of entrained particles may change the melt pool flow from symmetrical vortex flow to single vortex flow. The change of flow field directly influences the transport of metallic elements at the melt pool tail, which probably alters the element distribution at the top of melt track.

CRediT authorship contribution statement

Yanming Zhang: Conceptualization, Methodology, Investigation, Formal analysis, Data curation, Writing – original draft. **Shiwei Wu:** Experiments, Data curation. **Zixu Guo:** Experiments, Data curation. **Guochen Peng:** Experiments, Data curation. **Lu Wang:** Formal analysis, Data curation. **Wentao Yan:** Writing – review & editing, Supervision, Software, Resources, Project administration, Funding acquisition.

Declaration of competing interest

The authors declare that they have no known competing financial interests or personal relationships that could have appeared to influence the work reported in this paper.

Acknowledgments

The authors acknowledge the financial support by the Ministry of Education, Singapore under its Academic Research Fund Tier 2 (MOE-T2EP50121-0017) and by A*STAR, Singapore under its Advanced Models for Additive Manufacturing (AM2) programme (Award M22L2b0111). The authors acknowledge Zeshi Yang for his support of LPBF experiment. The authors acknowledge Hou Yi Chia for his suggestion on simulation analysis.

Appendix A. Supplementary data

Supplementary material related to this article can be found online at https://doi.org/10.1016/j.actamat.2025.120816.

References

[1] W.J. Sames, F. List, S. Pannala, R.R. Dehoff, S.S. Babu, The metallurgy and processing science of metal additive manufacturing, Int. Mater. Rev. 61 (5) (2016) 315–360.
[2] T. DebRoy, T. Mukherjee, J. Milewski, J. Elmer, B. Ribic, J. Blecher, W. Zhang, Scientific, technological and economic issues in metal printing and their solutions, Nat. Mater. 18 (10) (2019) 1026–1032.
[3] D. Gu, X. Shi, R. Poprawe, D.L. Bourell, R. Setchi, J. Zhu, Material-structure-performance integrated laser-metal additive manufacturing, Science 372 (6545) (2021).
[4] T. Zhang, Z. Huang, T. Yang, H. Kong, J. Luan, A. Wang, D. Wang, W. Kuo, Y. Wang, C.-T. Liu, In situ design of advanced titanium alloy with concentration modulations by additive manufacturing, Science 374 (6566) (2021) 478–482.
[5] G. Wang, Y. Zhang, B. Zou, Y. Liu, S. Zheng, X. Li, W. Yan, Z. Li, Y.M. Wang, Enhanced plasticity due to melt pool flow induced uniform dispersion of reinforcing particles in additively manufactured metallic composites, Int. J. Plast. 164 (2023) 103591.
[6] Y. Liu, J. Zhang, R. Niu, M. Bayat, Y. Zhou, Y. Yin, Q. Tan, S. Liu, J.H. Hattel, M. Li, et al., Manufacturing of high strength and high conductivity copper with laser powder bed fusion, Nat. Commun. 15 (1) (2024) 1283.
[7] M. Seifi, A. Salem, J. Beuth, O. Harrysson, J.J. Lewandowski, Overview of materials qualification needs for metal additive manufacturing, JOM 68 (2016) 747–764.
[8] Z. Chen, C. Han, M. Gao, S.Y. Kandukuri, K. Zhou, A review on qualification and certification for metal additive manufacturing, Virtual Phys. Prototyp. 17 (2) (2022) 382–405.
[9] Z. Snow, A.R. Nassar, E.W. Reutzel, Invited review article: Review of the formation and impact of flaws in powder bed fusion additive manufacturing, Addit. Manuf. 36 (2020) 101457.
[10] A. Mostafaei, C. Zhao, Y. He, S.R. Ghiaasiaan, B. Shi, S. Shao, N. Shamsaei, Z. Wu, N. Kouraytem, T. Sun, et al., Defects and anomalies in powder bed fusion metal additive manufacturing, Curr. Opin. Solid State Mater. Sci. 26 (2) (2022) 100974.
[11] M.J. Matthews, G. Guss, S.A. Khairallah, A.M. Rubenchik, P.J. Depond, W.E. King, Denudation of metal powder layers in laser powder bed fusion processes, Acta Mater. 114 (2016) 33–42.
[12] S. Ly, A.M. Rubenchik, S.A. Khairallah, G. Guss, M.J. Matthews, Metal vapor micro-jet controls material redistribution in laser powder bed fusion additive manufacturing, Sci. Rep. 7 (1) (2017) 4085.
[13] U. Ali, R. Esmaeilizadeh, F. Ahmed, D. Sarker, W. Muhammad, A. Keshavarzkermani, Y. Mahmoodkhani, E. Marzbanrad, E. Toyserkani, Identification and characterization of spatter particles and their effect on surface roughness, density and mechanical response of 17-4 ph stainless steel laser powder-bed fusion parts, Mater. Sci. Engineering: A 756 (2019) 98–107.
[14] R. Esmaeilizadeh, U. Ali, A. Keshavarzkermani, Y. Mahmoodkhani, E. Marzbanrad, E. Toyserkani, On the effect of spatter particles distribution on the quality of hastelloy X parts made by laser powder-bed fusion additive manufacturing, J. Manuf. Process. 37 (2019) 11–20.
[15] C. Schwerz, A. Raza, X. Lei, L. Nyborg, E. Hryha, H. Wirdelius, In-situ detection of redeposited spatter and its influence on the formation of internal flaws in laser powder bed fusion, Addit. Manuf. 47 (2021) 102370.
[16] Z. Snow, L. Scime, A. Ziabari, B. Fisher, V. Paquit, Observation of spatter-induced stochastic lack-of-fusion in laser powder bed fusion using in situ process monitoring, Addit. Manuf. 61 (2023) 103298.
[17] P. Bidare, I. Bitharas, R. Ward, M. Attallah, A.J. Moore, Fluid and particle dynamics in laser powder bed fusion, Acta Mater. 142 (2018) 107–120.
[18] C. Zhao, N.D. Parab, X. Li, K. Fezzaa, W. Tan, A.D. Rollett, T. Sun, Critical instability at moving keyhole tip generates porosity in laser melting, Science 370 (6520) (2020) 1080–1086.
[19] M. Qu, Q. Guo, L.I. Escano, A. Nabaa, S.M.H. Hojjatzadeh, Z.A. Young, L. Chen, Controlling process instability for defect lean metal additive manufacturing, Nat. Commun. 13 (1) (2022) 1079.
[20] Y. Huang, T.G. Fleming, S.J. Clark, S. Marussi, K. Fezzaa, J. Thiyagalingam, C.L.A. Leung, P.D. Lee, Keyhole fluctuation and pore formation mechanisms during laser powder bed fusion additive manufacturing, Nat. Commun. 13 (1) (2022) 1170.
[21] I. Bitharas, N. Parab, C. Zhao, T. Sun, A. Rollett, A. Moore, The interplay between vapour, liquid, and solid phases in laser powder bed fusion, Nat. Commun. 13 (1) (2022) 2959.
[22] H. Chen, Q. Wei, Y. Zhang, F. Chen, Y. Shi, W. Yan, Powder-spreading mechanisms in powder-bed-based additive manufacturing: Experiments and computational modeling, Acta Mater. 179 (2019) 158–171.
[23] W. Yan, W. Ge, Y. Qian, S. Lin, B. Zhou, W.K. Liu, F. Lin, G.J. Wagner, Multi-physics modeling of single/multiple-track defect mechanisms in electron beam selective melting, Acta Mater. 134 (2017) 324–333.
[24] M. Bayat, A. Thanki, S. Mohanty, A. Witvrouw, S. Yang, J. Thorborg, N.S. Tiedje, J.H. Hattel, Keyhole-induced porosities in laser-based powder bed fusion (L-PBF) of Ti6Al4V: High-fidelity modelling and experimental validation, Addit. Manuf. 30 (2019) 100835.
[25] L. Wang, Y. Zhang, H.Y. Chia, W. Yan, Mechanism of keyhole pore formation in metal additive manufacturing, Npj Comput. Mater. 8 (1) (2022) 1–11.
[26] Q. Zhu, J. Yan, A mixed interface-capturing/interface-tracking formulation for thermal multi-phase flows with emphasis on metal additive manufacturing processes, Comput. Methods Appl. Mech. Engrg. 383 (2021) 113910.
[27] S.A. Khairallah, A.A. Martin, J.R. Lee, G. Guss, N.P. Calta, J.A. Hammons, M.H. Nielsen, K. Chaput, E. Schwalbach, M.N. Shah, et al., Controlling interdependent meso-nanosecond dynamics and defect generation in metal 3D printing, Science 368 (6491) (2020) 660–665.
[28] X. Li, Q. Guo, L. Chen, W. Tan, Quantitative investigation of gas flow, powder-gas interaction, and powder behavior under different ambient pressure levels in laser powder bed fusion, Int. J. Mach. Tools Manuf. (2021) 103797.
[29] T. Yu, J. Zhao, Quantitative simulation of selective laser melting of metals enabled by new high-fidelity multiphase, multiphysics computational tool, Comput. Methods Appl. Mech. Engrg. 399 (2022) 115422.
[30] W. Yuan, H. Chen, C. Peng, R. Lupoi, S. Yin, Revealing melt-vapor-powder interaction towards laser powder bed fusion process via DEM-CFD coupled model, Surf. Sci. Technol. 1 (1) (2023) 14.
[31] M. Manninen, V. Taivassalo, S. Kallio, On the mixture model for multiphase flow, 1996.
[32] J. Ahn, S.-J. Na, Three-dimensional thermal simulation of nanosecond laser ablation for semitransparent material, Appl. Surf. Sci. 283 (2013) 115–127.
[33] V.A. Markel, Introduction to the maxwell garnett approximation: tutorial, J. Opt. Soc. Amer. A 33 (7) (2016) 1244–1256.
[34] C.W. Hirt, B.D. Nichols, Volume of fluid (VOF) method for the dynamics of free boundaries, J. Comput. Phys. 39 (1) (1981) 201–225.

[35] L. Wang, Y. Zhang, W. Yan, Evaporation model for keyhole dynamics during additive manufacturing of metal, Phys. Rev. Appl. 14 (6) (2020) 064039.
[36] S. Popinet, An accurate adaptive solver for surface-tension-driven interfacial flows, J. Comput. Phys. 228 (16) (2009) 5838–5866.
[37] B. Keene, Review of data for the surface tension of pure metals, Int. Mater. Rev. 38 (4) (1993) 157–192.
[38] Z. Yang, Y. Zhang, W. Yan, High-fidelity modeling of binder–powder interactions in binder jetting: Binder flow and powder dynamics, Acta Mater. 260 (2023) 119298.
[39] C. Crowe, M. Sommerfeld, Y. Tsuji, et al., Multiphase flows with, 1998.
[40] H.R. Norouzi, R. Zarghami, R. Sotudeh-Gharebagh, N. Mostoufi, Coupled CFD-DEM modeling: formulation, implementation and application to multiphase flows, John Wiley & Sons, 2016.
[41] H. Chen, W. Yan, Spattering and denudation in laser powder bed fusion process: Multiphase flow modelling, Acta Mater. 196 (2020) 154–167.
[42] J. Welty, G.L. Rorrer, D.G. Foster, Fundamentals of momentum, heat, and mass transfer, John Wiley & Sons, 2014.
[43] J. López, J. Hernández, P. Gómez, F. Faura, VOFTools- a software package of calculation tools for volume of fluid methods using general convex grids, Comput. Phys. Comm. 223 (2018) 45–54.
[44] A. van de Walle, C. Nataraj, Z.-K. Liu, The thermodynamic database database, CALPHAD 61 (2018) 173–178.
[45] B. Sundman, H. Lukas, S. Fries, Computational thermodynamics: the calphad method, Cambridge university press Cambridge, 2007.
[46] I. Bitharas, A. Burton, A. Ross, A. Moore, Visualisation and numerical analysis of laser powder bed fusion under cross-flow, Addit. Manuf. 37 (2021) 101690.
[47] X. Zhang, B. Cheng, C. Tuffile, Simulation study of the spatter removal process and optimization design of gas flow system in laser powder bed fusion, Addit. Manuf. 32 (2020) 101049.
[48] Z.A. Young, Q. Guo, N.D. Parab, C. Zhao, M. Qu, L.I. Escano, K. Fezzaa, W. Everhart, T. Sun, L. Chen, Types of spatter and their features and formation mechanisms in laser powder bed fusion additive manufacturing process, Addit. Manuf. 36 (2020) 101438.
[49] S.M.H. Hojjatzadeh, N.D. Parab, W. Yan, Q. Guo, L. Xiong, C. Zhao, M. Qu, L.I. Escano, X. Xiao, K. Fezzaa, et al., Pore elimination mechanisms during 3D printing of metals, Nat. Commun. 10 (1) (2019) 3088.
[50] C. Zhao, B. Shi, S. Chen, D. Du, T. Sun, B.J. Simonds, K. Fezzaa, A.D. Rollett, Laser melting modes in metal powder bed fusion additive manufacturing, Rev. Modern Phys. 94 (4) (2022) 045002.
[51] A.R. Miedema, F.J.d. Broeder, On the interfacial energy in solid-liquid and solid-solid metal combinations, Int. J. Mater. Res. 70 (1) (1979) 14–20.
[52] C. Guo, Z. Xu, Y. Zhou, S. Shi, G. Li, H. Lu, Q. Zhu, R.M. Ward, Single-track investigation of IN738lc superalloy fabricated by laser powder bed fusion: Track morphology, bead characteristics and part quality, J. Mater. Process. Technol. 290 (2021) 117000.
[53] Y. He, M. Zhong, J. Beuth, B. Webler, A study of microstructure and cracking behavior of H13 tool steel produced by laser powder bed fusion using single-tracks, multi-track pads, and 3D cubes, J. Mater. Process. Technol. 286 (2020) 116802.
[54] A. Gaikwad, B. Giera, G.M. Guss, J.-B. Forien, M.J. Matthews, P. Rao, Heterogeneous sensing and scientific machine learning for quality assurance in laser powder bed fusion–a single-track study, Addit. Manuf. 36 (2020) 101659.
[55] W.F. Templeton, S. Hinnebusch, S. Strayer, A. To, S.P. Narra, Finding the limits of single-track deposition experiments: an experimental study of melt pool characterization in laser powder bed fusion, Mater. Des. 231 (2023) 112069.
[56] F. Chu, E. Li, H. Shen, Z. Chen, Y. Li, H. Liu, S. Min, X. Tian, K. Zhang, Z. Zhou, et al., Influence of powder size on defect generation in laser powder bed fusion of AlSi10Mg alloy, J. Manuf. Process. 94 (2023) 183–195.
[57] D. Simson, S.K. Subbu, Investigation of build strategies for microfeatures fabrication using laser powder bed fusion, J. Manuf. Process. 79 (2022) 990–1002.
[58] S. Huang, R.L. Narayan, J.H.K. Tan, S.L. Sing, W.Y. Yeong, Resolving the porosity-unmelted inclusion dilemma during in-situ alloying of Ti34Nb via laser powder bed fusion, Acta Mater. 204 (2021) 116522.
[59] S. Pilz, T. Gustmann, F. Günther, M. Zimmermann, U. Kühn, A. Gebert, Controlling the Young's modulus of a ß-type Ti-Nb alloy via strong texturing by LPBF, Mater. Des. 216 (2022) 110516.
[60] M. Liu, J. Zhang, C. Chen, Z. Geng, Y. Wu, D. Li, T. Zhang, Y. Guo, Additive manufacturing of pure niobium by laser powder bed fusion: Microstructure, mechanical behavior and oxygen assisted embrittlement, Mater. Sci. Engineering: A 866 (2023) 144691.
[61] L. Wang, Z. Guo, G. Peng, S. Wu, Y. Zhang, W. Yan, Evaporation-induced composition evolution in metal additive manufacturing, Adv. Funct. Mater. (2024) 2412071.